Biophysical Studies on Protein–Protein Interactions in Drug Discovery

January 2019

Yusuke KAMADA

Biophysical Studies on Protein–Protein Interactions in Drug Discovery

A Dissertation Submitted to

the Graduate School of Life and Environmental Sciences,

the University of Tsukuba

in Partial Fulfillment of the Requirements

for the Degree of Doctor of Philosophy in Biological Science

(Doctoral Program in Biological Sciences)

Yusuke KAMADA

Table of Contents

Abstract 6

Abbreviations 8

General Introduction 12

Chapter I:Discovery of a B-Cell Lymphoma 6 Protein–Protein Interaction Inhibitor by a Biophysics-Driven Fragment-Based Approach 19

Abstract 20

Introduction 21

Materials & Methods 22

Results 27

Discussion 32

Chapter II: Discover of K-Ras(G12D)-Selective Inhibitory Peptide by Random Peptide T7 Phage Display Technology and Its Structural Characterization 50

Abstract 51

Introduction 52

Materials & Methods 54

Results 61

Discussion 67

Tables & Figures 72

General Discussion 92

Acknowledgements 98

References 100

Abstract

Protein–protein interactions (PPIs) are central to the control of all biological processes. Therefore, studies of PPI inhibitors are critical for the progress of biological sciences and drug discovery. However, PPIs are commonly regarded as intractable targets because they do not possess small cavities for small molecule binding, and interfacing surfaces of PPIs are often large and flat.

The objective of this study was to identify PPI inhibitors and elucidate the mechanisms of their interactions using biophysical methods that are feasible for the discovery of compounds that inhibit PPIs. To identify PPI inhibitors, I used a screening method that exploits PPI properties. In chapter I, I report fragment-based screening against B-cell lymphoma 6 (BCL6), which interacts with BCL6 corepressor (BCoR) and has predicted hot spots. In chapter II, I present a phage display screen against V-Ki-ras2 Kirsten rat sarcoma viral oncogene homolog (K-Ras), which interacts with son of sevenless 1 (SOS1) and causes conformational changes. These screens led to the discovery of active inhibitors against 2 PPI targets. The resulting compounds have unique properties and can binding to hot spots and allosteric sites, indicating that PPIs can be considered a drug target class during the early stages of drug discovery. Finally, I suggest a work-flow for discovering PPI inhibitors on the basis of the evidence presented herein. This study is a contribution to drug discovery research and biology, and the reported methods could be exploited to discover novel compounds against other PPIs.

Abbreviations

BCL2	B-cell lymphoma 2
BCL6	B-cell lymphoma 6
BCoR	BCL6 corepressor
DMSO	dimethyl sulfoxide
DTT	dithiothreitol
EDTA	ethylenediaminetetraacetic acid
ELISA	enzyme-linked immunosorbent assay
Et_3N	triethylamine
EtOAc	ethylacetate
EtOH	ethanol
FADD	fragment-assisted drug discovery
FBDD	fragment-based drug discovery
FRET	fluorescence resonance energy transfer
Fsp^3	fraction sp^3
GAP	GTPase-activating protein
GDP	guanosine 5'-diphosphate
GEF	guanine nucleotide exchange factor
GPCR	G-protein coupled receptor
GST	glutathione S-transferase

GTP	guanosine 5'-triphosphate
HPLC	high-performance liquid chromatography
HTS	high throughput screening
IPE	diisopropyl ether
i-PrOH	2-propanol
ITC	isothermal titration calorimetry
K-Ras	V-Ki-ras2 Kirsten rat sarcoma viral oncogene homolog
LE	ligand efficiency
M2H	mammalian two hybrid assay
MeCN	acetonitrile
MeOH	methanol
MS	mass spectrometry
MT	mutant
NCoR	nuclear receptor corepressor
NMR	nuclear magnetic resonance
NMP	N-methyl-2-pyrrolidone
PAINS	pan-assay interference compounds
PCR	polymerase chain reaction
PPI	protein-protein interaction

RBD	Raf-Ras binding domain
RU	resonance unit
SA	streptavidin
SAR	structural-activity relationships
SBDD	structure based drug design
SMART	silencing mediator of retinoic acid and thyroid hormone receptor
SOS	son of sevenless
SPR	surface plasmon resonance
STD	saturation transfer difference
TEA	triethylamine
TEV	Tabacco etch virus
TFA	trifluoroacetic acid
TSA	thermal shift assay
WT	wild-type

General Introduction

1. Importance of PPIs in drug discovery and biological sciences

PPIs are central to the control of biological processes,[1] and compounds that can selectively inhibit PPIs could be used to investigate biological systems in chemical and biological analyses. PPI inhibitors that are related to diseases could also directly lead to drug discovery. Therefore, studies of PPI inhibitors will greatly facilitate the progress of biological sciences and drug discovery. However, PPIs are commonly regarded as intractable targets because they do not carry cavities for small molecule binding, and their interfacing surfaces are often flatter and larger than traditional drug targets, such as enzymes and GPCRs.[2]

Since the 1990s, large pharmaceutical companies have generally conducted HTS using combinations of chemical compound libraries and biochemical assays on microplates to discover novel drugs. Whereas these HTS methods are suitable for enzymes and GPCRs, which have small pockets where small molecules tend to bind, they have so far failed to provide validated potential compounds that inhibit PPIs. Thus, to overcome these hurdles, pharmaceutical companies and academic institutions have developed screening methodologies and compound libraries.

With regard to screening methodologies, biophysical techniques that directly detect binding of compounds would be more feasible for PPIs, because these have higher sensitivity and greater accuracy than biochemical assays.[3] Moreover, to generate compound libraries, fragments, high Fsp^3 compounds, and peptides may offer the most feasible approaches for PPIs,[4-6] because fragments have good physicochemical properties and vast chemical diversity, high Fsp^3 compounds are adjustable for various PPIs surfaces, and peptides are flexible for dynamic PPIs. In 2016, the BCL2 inhibitor Venetoclax was launched as the first small molecule PPI inhibitor that was discovered from a screen

of library compounds.[7] This progress has motivated further research in this area, and the ensuing discoveries of PPI inhibitors are expected to contribute to drug discovery. However, more rational strategies may be required to discover PPI inhibitors because the success of Venetoclax may reflect serendipitous conditions compared with traditional target classes.

2. Evidence of PPIs as drug targets

2-1. Classification of PPIs

Previous drug discovery studies have been directed at classifying PPIs, and among these, Smith and colleagues classified PPIs with buried surface areas and defined the affinities of their inhibitors.[8] They also classified known PPIs into tight narrow, tight wide, loose narrow, and loose wide categories with standards of 2500 $Å^2$ for buried surface areas and 200 nM for affinity. Some inhibitors of tight narrow, tight wide, and loose narrow types have been identified using conventional HTS, whereas only Ras–SOS interactions have been classified as loose wide, indicating that drug discovery of PPI targets in the loose wide category is extremely challenging. Hence, the discovery of inhibitors for PPI targets of this category will require more sophisticated strategies.

Arkin and colleagues previously classified PPIs with epitopes of their partner proteins[9] and described primary peptide, secondary structure, and tertiary structure classifications of PPIs. High affinity inhibitors against PPIs of the primary peptide category tend to be discovered readily. Among these, several bromodomain inhibitors have been considered for clinical trials, including Apabetalne and GSK525762. In contrast, PPIs of the other types are refractory to the generation of compounds that are worthy of clinical trials. Over 60% of PPIs in the PDB are classified as secondary-structure interactions.[10-11] Whereas conventional HTS have revealed PPI inhibitors of the secondary-

structure type, these inhibitors have poor affinity compared with those of the primary-peptide category. The discovery of compounds that can interact with PPIs of tertiary structure remains extremely difficult using HTS, and further approaches are necessary to find inhibitors for this category of PPIs. In addition to the above-mentioned classifications, Duncan and colleagues classified PPIs from the perspective of recognition structures of proteins as follows: globular–globular, globular–peptide, and peptide–peptide.[12] These investigators suggested that drug discovery approaches employing FBDD and *in silico* screening of apo-structures will likely fail to reveal PPIs that undergo conformational changes during their interactions.

2-2. Discovery of various PPI disrupters in basic research

Previous studies have generated various kinds of compounds that inhibit PPIs.[6] In addition to orthostatic and allosteric inhibitors, PPI regulators with new mechanisms have been found. [13] Among these, stabilizers disrupt PPI signals by stabilizing PPIs, as reviewed comprehensively by Ottmann and colleagues.[14]

2-3. Hot spots

Hot spots are a type of structure that occurs in interaction surfaces of PPIs, and provide most of the binding free energy in PPIs. Mutational analysis using an alanine scanning technique identified hot spots on both sides of PPIs. These tended to comprise hydrophobic residues at a central site with hydrophilic residues peripherally.[15-16] These distinctive structures likely limit access of water molecules to central hydrophobic sites and contribute to the binding free energy, as demonstrated by DeLano and colleagues with the proteins Fc and IgG.[17] Accordingly, compounds that bind hot spots would likely do so with high affinity, because hot spots are much smaller than buried surface areas of PPIs, thus facilitating binding of small molecules.[18] The above-mentioned compound Venetoclax

was optimized from several fragments that bind to hot spots, which were identified using NMR screening, which is a biophysical method.

3. Biophysics

3-1. Biophysical techniques and roles in drug discovery

Biophysical analyses provide detailed information about interactions among compounds, proteins, and other molecules and can be used to determine binding affinities, kinetics, thermodynamics, and structures. Such biophysical techniques include NMR, SPR, ITC, TSA, and X-ray spectral analyses, and in drug discovery, these are often used to validate hits and remove false positives of HTS.[3, 19-20] Recent studies have also used the interaction parameters obtained using biophysical techniques to investigate medicinal chemistry and pharmacokinetics.[21-22]

3-2. Applications to compound screening

As the roles of biophysics in drug discovery increase, sensitivity and throughput of the required instrumentation has been improved.[19] In the following sections, these concepts are exemplified in applications of biophysics to compound screening, particularly with an introduction to fragment-based and phage display screening.

3-2-1. Fragment-based screening

FBDD has been widely practiced in both industry and academia to identify novel scaffolds, binding sites, and compounds with good physiological profiles.[23] Initially, molecule fragments with low affinity are identified using high concentration screening and their affinities are then improved by linking or growing them. Biophysical methods such as SPR, NMR, and thermal shift assays have been used in FBDD because they are more sensitive than biochemical assays.[24-25] Of these, SPR biosensing is the most cost-effective and widely used, with low protein

consumption and quick assay development. This technique provides high-content information on binding affinities and kinetics, and can be used to identify PAINS. PPIs represent a challenging target for biophysics-driven FBDD approaches because the targets do not have deep binding pockets.[18, 26]

3-2-2. Phage display screening

Phage display screening is one of the most powerful techniques for generating peptides that bind to target proteins, and is performed using phage display libraries that are constructed by bacteriophages displaying > 10 billion distinct peptides on their outer surfaces. In these procedures, phages that bind target proteins are isolated from the libraries using an affinity selection technique called biopanning, and the displayed amino acid sequences are deduced by sequencing DNA from bound phages. Because false positives occur frequently when identifying peptides from phages, biophysical techniques are required to directly determine binding of peptides to target proteins, and thereby identify false positives. In combination with these methods, phage display screening generates peptides with high affinity, selectivity, and allostery for target proteins, reflecting large and diverse libraries. Several peptides have been discovered using phage display screening against various target classes, including PPIs.[27-29]

4. Objective of this study

The objective of this study was to identify PPI inhibitors and investigate their interactions using biophysical techniques, and then identify candidate PPI-inhibitory compounds. To identify PPI inhibitors, I conducted a screening method that is suitable for PPI properties.

Initially, 1) FBDD was performed for PPIs with hot spots using a compound library comprising various small fragmented compounds. 2) Phage display screening was then performed using discovery peptides for PPIs that are

not affected by hot spots and instead interact via conformational changes. In these experiments, binding modes of selected compounds were elucidated from binding analyses using SPR and X-ray crystallography.

The results of these studies show that compounds can be generated against individual PPIs to identify potential drugs, and that if optimal strategies can be predicted based on the properties of specific PPIs properties, significant contributions to drug discovery research and biology will be made.

Chapter I:

Discovery of a B-Cell Lymphoma 6 Protein–Protein Interaction Inhibitor by a Biophysics-Driven Fragment-Based Approach

Abstract

B-cell lymphoma 6 (BCL6) is a transcriptional factor that expresses in lymphocytes and regulates the differentiation and proliferation of lymphocytes. Therefore, BCL6 is a therapeutic target for autoimmune diseases and cancer treatment. This chapter presents the discovery of BCL6-corepressor interaction inhibitors by using a biophysics-driven fragment-based approach. Using the surface plasmon resonance (SPR)-based fragment screening, I successfully identified fragment **1** (SPR K_D = 1200 μM, ligand efficiency (LE) = 0.28), a competitive binder to the natural ligand BCoR peptide. Moreover, I elaborated **1** into the more potent compound **7** (SPR K_D = 0.078 μM, LE = 0.37, cell-free protein-protein interaction (PPI) IC_{50} = 0.48 μM (ELISA), cellular PPI IC_{50} = 8.6 μM (M2H)) by a structure-based design and structural integration with a second high-throughput screening hit.

Introduction

BCL6 is a transcriptional factor that belongs to the bric-a-brac, tramtrack, broad complex/poxvirus zinc finger (BTB/POZ) family of proteins. It has BTB, RD2, and zinc finger domains and interacts with three corepressors, i.e., BCoR, SMRT, and NCoR.[30] It drives germinal center B-cell formation and differentiation of T lymphocytes.[31-34] It is also involved in the differentiation and proliferation of diffuse large B-cell lymphomas.[35-36] Consequently, it is thought to be a potent therapeutic target for the treatment of autoimmune diseases and cancer.

The crystal structure of the BCL6 BTB domain ($BCL6^{BTB}$) complexed with the SMRT peptide has already been reported.[37] The crystal structure of the cocomplex with the BCL6 inhibitor 79-6 has also been solved.[38] These ligands bind in the lateral groove of the $BCL6^{BTB}$ homodimer. Parekh et al. have suggested that the lateral groove of the $BCL6^{BTB}$ homodimer could be an effective therapeutic target to develop effective small-molecule inhibitors.[35] Several compounds and peptides, other than 79-6, have been reported as $BCL6^{BTB}$ inhibitors, including RI-BPI with a K_D of ~10 μM, Rifamycin SV with a K_D of ~1 mM, and FX1 with a K_D of 7 μM, all of which have binding affinities weaker than 1 μM (Figure 1-1).[39-41] Recently, I reported the peptide F1324, which inhibits the BCL6-BCoR interaction with a K_D of 0.57 nM (Figure 1-1).[28] Peptide F1324 also binds to the lateral groove of the $BCL6^{BTB}$ homodimer. These data suggest that the lateral groove of the $BCL6^{BTB}$ homodimer could be a potent site for inhibitors to bind with high affinity.

In this study, SPR-based fragment screening was performed against BCL6 to discover BCL6-cofactor interaction inhibitors. As a result, I successfully found triazine fragment **1**, which binds to the lateral groove of the $BCL6^{BTB}$ homodimer where BCoR also binds. Furthermore, fragment **1** was elaborated into the more potent inhibitor

7, which exhibits cellular activity and two-digit nanomolar binding affinity, by structure-based drug design using X-ray analysis and structural integration with a second HTS hit. This process represents a highly successful FADD.[42-43]

Materials & Methods

Preparation of BCL6.

The fragments of His, avi, SUMO (LifeSensors), Flag, TEV protease recognition sequence, and $BCL6^{BTB}$ (human BCL6 from 5 to 129 aa) were amplified by the PCR and ligated into pET21 vector (Merck). The MT $BCL6^{BTB}$ (C8Q, C67R, C84N) was constructed by the overlap PCR method. The proteins were expressed in *E. coli* BL21 (DE3) (NIPPON GENE) and partially biotinylated on avi-tag by endogenous BirA. The proteins were purified using Ni-NTA (QIAGEN) and Superdex200 (GE healthcare) columns. For Flag-tagged WT $BCL6^{BTB}$, SUMO was digested by ULP1 (LifeSensors). To remove ULP1, His-avi-SUMO, and uncleaved protein, the digested solution was passed through an Ni-NTA column in 50 mM Tris-HCl pH 8.0, 300 mM NaCl, 5% glycerol, and 1 mM DTT. To increase the purity, ion-exchange chromatography (monoQ, GE Healthcare) was conducted. The purified proteins were concentrated to 2 mg/mL for storage at −80°C.

Fragment Library.

The library contained 1494 fragments. All fragments in the library had a clogP <3.5, the number of Hydrogen-bond acceptors and donors were <6 and <3 respectively, and rotatable bonds were <3. Heavy atom count ranged between 8 and 15. The molecular weight of the fragments was <350 Da (average 180 Da), and the average of

the aromatic rings was 1.5. Fragments were dissolved at 200 mM in 100% DMSO and stored at −30 °C.

SPR.

SPR biosensing experiments were performed at 22°C on Biacore 4000 and Biacore S200 instruments equipped with SeriesS CM5 and SA sensor chips (GE healthcare). HBS-P+ (10 mM Hepes pH 7.4, 150 mM NaCl, 0.05% Surfactant P20, GE healthcare) supplemented with 1 mM DTT was used as the running buffer for immobilization. NeutrAvidin (Thermo Fisher Scientific Inc.) was covalently coupled onto spots 1, 2, and 3 of a CM5 sensor chip following the standard amine coupling procedure according to the manufacturer's instructions. Typical immobilization levels of NeutrAvidin ranged from 10,000 to 13,000 resonance units (RUs). Subsequently, avi-tagged WT $BCL6^{BTB}$ and avi-tagged MT $BCL6^{BTB}$ were injected to spots 1 and 2, respectively. The surfaces were blocked by injecting biocytin (Thermofisher) to spots 1, 2, and 3. Approximately 13,000 RUs of each $BCL6^{BTB}$ were captured by NeutrAvidin. Furthermore, WT $BCL6^{BTB}$ was immobilized on spot 5 via the standard amine coupling procedure, resulting in immobilization levels of around 4,000 RUs.

For the interaction studies, binding experiments were performed in 20 mM Tris, pH 8.0, 150 mM NaCl, 0.01% Surfactant P20, 1 mM DTT, and 5% DMSO. Different concentration sample solutions were injected for 30 or 60 s at a flow rate of 30 or 50 µL/min, and the dissociation was thereafter followed for up to 30, 60, or 150 s. Data processing and analysis were performed using the Biacore 4000 and Biacore S200 evaluation software (GE healthcare). Solvent correction was included as described in the Biacore software handbook. Sensorgrams were double referenced prior to fitting the concentration series to a steady-state affinity model. The dissociation constant K_D was calculated using the equation:

$K_D = R_{max} \times C/R - C$

where R_{max}, R, and C correspond to the sample binding capacity of the surface (RU), the normalized response of test sample (RU), and the concentration of the test solution (M), respectively. LE was calculated using the equation:

$LE = \Delta G/HA = (-2.303 \times R \times T) \times \log (K_D)/HA$

where ΔG, HA, R, and T correspond to the Gibbs free energy (kcal/mol), heavy atom count, the ideal gas constant (1.987×10^{-3} kcal/K/mol) and the temperature in Kelvin (K).[44]

For the primary screen, Takeda's fragment library was diluted to 1 mM in the running buffer and injected for 30 s. Then, the dissociation was followed for 30 s. Every 33rd cycle, a positive control containing 100 μM BCoR peptide ((Arg498-Pro514)-Lys, acetyl-RSEIISTAPSSWVVPPK-OH, chemically synthesized by Toray Research Center) and running buffer as a blank were injected. Data processing and analysis were performed using the Biacore 4000 evaluation software. Solvent correction was included as described in the Biacore 4000 software handbook. The binding responses were normalized by the positive control and the molecular weight of each sample. Fragments with a normalized binding response that exceeded median + median absolute deviation were selected as primary hits. As for NeutrAvidin, fragments with a normalized response that was more than 90% against their theoretical R_{max} were selected.

For competition studies, data were acquired for test compounds binding to BCL6 in the presence of 100 μM BCoR peptide in the running buffer and samples. When a compound binds to the same site as the BCoR peptide, the response for the compound decreases.[45]

X-ray Crystallography.

Crystals of unliganded $BCL6^{BTB}$ for soaking experiments were obtained as described previously.[28] Crystallization was by vapor-diffusion using the sitting-drop method from 0.1 M Bis-Tris pH 6.5, 0.7 M potassium/sodium tartrate at 20°C. To generate protein-ligand complexes, crystals were typically soaked for 2 h in a reservoir solution containing 1 mM ligand(s). Prior to data collection, crystals were immersed in the reservoir solution with the addition of 30% glycerol as a cryoprotectant and were flash-frozen in liquid nitrogen. Diffraction data were collected from a single crystal using the CCD detector Quantum 315 (ADSC) at beamlines 5.0.2 and 5.0.3 of the Advanced Light Source (Berkeley) under a 100 K nitrogen cryostream. The data were reduced and scaled with HKL2000.[46] The structures were solved by the molecular replacement method with Molrep[47] of the CCP4 software suite[48] using the $BCL6^{BTB}$ structure (PDB code: 1R28) as a search model. The structures were refined through an iterative procedure utilizing REFMAC,[49] followed by model building in COOT.[50] The final models were validated using Molprobity.[51] Crystallographic processing and refinement statistics are summarized in Table 1-4. All structural figures were generated using PyMOL (Schrödinger).

STD-NMR.

^{1}H NMR spectra were recorded using a 3 mm NMR tube on a 600 MHz Avance spectrometer (Bruker Biospin) equipped with a 5 mm TCI cryoprobe. All NMR samples were prepared in 50 mM phosphate D_2O buffer at pH 7.4 containing 150 mM NaCl, 1 mM DTT-d_{10}, and 0.2% DMSO-d_6 in D_2O solvent. The STD spectrum was acquired from a sample containing 400 µM of fragment **1** and 20 µM $BCL6^{BTB}$ at 15°C with 32 scans with on- and off-resonance saturation frequencies of 0.4 and 30 ppm, respectively, and a total saturation time of 2.0 s. The decrease in signal intensity for on-resonance irradiation results from the transfer of saturation from $BCL6^{BTB}$ to fragment **1**.

The STD spectrum of fragment **1** was obtained by subtracting the on-resonance spectrum from the off-resonance spectrum. A positive signal in the STD spectrum indicates binding of fragment **1** to $BCL6^{BTB}$.

ELISA.

Biotinylation of the ε-amino group of the C-terminus Lys on the BCoR peptide was carried out with the Biotin-$(AC_5)_2$ Sulfo-OSu (DOJINDO) according to the protocol recommended by the manufacturer. The wells of a Nunc Maxisorp microplate (460-518) were coated with SA (Wako) and were blocked with phosphate-buffered saline (PBS) that contained 1.0% Casein. The biotinylated BCoR peptide was captured by the SA, and a WT $BCL6^{BTB}$ (0.5 nM) solution in PBS that contained 0.05% Tween20 and 1 mM DTT (PBST) was added to the wells. After washing with PBST, bound $BCL6^{BTB}$ was detected using horseradish peroxidase (HRP)-conjugated anti-FLAG antibody (Sigma). The amounts of HRP in the wells were measured using a chemical luminescent regent (Thermo Fisher Scientific Inc.).[28] Percent inhibition was calculated based on wells without $BCL6^{BTB}$ as a high control and without compound as a low control.

M2H.

The assay was performed according to a procedure described previously.[30] The vectors pGL4.35, pBind, and pACT were obtained from Promega Corp. As template DNA, human BCL6 cDNA was isolated by PCR from a human skeletal muscle cDNA library (TAKARA Bio), and human BCoR cDNA was purchased from GeneCopoeia Inc. Each cDNA fragment was granted a restriction site by PCR and digested with restriction enzymes to insert into pBIND or pACT, respectively. M2H was performed in HEK293T cells that were transfected with the reporter constructs pGL4.35 containing GAL4 special response element of firefly luciferase (9×GAL4UAS); pBIND/GAL4-

BCL6 (Ala5–Glu129); and pACT/VP16-BCoR (Leu112–Ala753) by Fugene HD (Promega). The transfected cells were seeded at 1×10^4 cells/15 μL/well on 384-well plates (CORNNING) in Dulbecco's modified Eagle's medium that contained 10% fetal bovine serum. After incubation for 20 h at 37°C under 5% CO_2, cells were lysed to measure luciferase activity using the Bright-Glo luciferase assay system (Promega).[28] Percent inhibition was calculated based on the well without transfection of pBIND/GAL-BCL6 (Ala5–Glu129) as the high control and the well without the compound as a low control.

Results

SPR Assay Development.

For my SPR-based screening, I used a Biacore 4000 high-throughput instrument with five detection areas for protein immobilization and four flow cells for compound injection. This parallel immobilization enables the evaluation of selectivity and nonspecific binding simultaneously.[52-54] I also screened against both wild-type (WT (Ala5-Glu129)) and mutant (MT (Ala5-Glu129, C8Q, C67R, and C84N)) $BCL6^{BTB}$ by SPR. Figure 1-2A, 1-2B shows the layout of the sensor chip used in this screening. Avi-tagged WT $BCL6^{BTB}$ and avi-tagged MT $BCL6^{BTB}$ were captured onto spots 1 and 2, respectively, by NeutrAvidin. In addition, WT $BCL6^{BTB}$ was covalently immobilized onto spot 5 by an amine coupling reaction (Figure 1-2). This configuration enabled us to evaluate binding to captured WT $BCL6^{BTB}$, captured MT $BCL6^{BTB}$, coupled WT $BCL6^{BTB}$, and coupled NeutrAvidin.

To verify the activity of each immobilized $BCL6^{BTB}$, I evaluated the binding of the BCoR peptide as a positive control (Figure 1-3C to 1-3F). The BCoR peptide successfully binds with each $BCL6^{BTB}$ in a dose-dependent manner.

The K_D values for the BCoR peptide with each BCL6^{BTB} are in the two-digit micromolar range. Since there are no significant differences in the binding affinities among the different BCL6^{BTB}s, the mutation of the Cys residues is not thought to affect the interaction between BCL6 and BCoR, and I concluded that each BCL6^{BTB} is immobilized while retaining its activity.

For performing high-quality SPR-based screening, maintaining the stability of the immobilized protein is important.[55-57] Therefore, selection of a suitable buffer is critical to retain stability. Compared with that used in biochemical assays, the concentration of DMSO required for SPR-based screening is generally higher to solubilize the fragments at high concentration. Accordingly, the influence of DMSO on the activities of the immobilized BCL6^{BTB}s was evaluated (Table 1-1 and Figure 1-4). The K_D and R_{max} values for the BCoR peptide are unaffected by the concentration of DMSO. Moreover, both WT BCL6^{BTB} and MT BCL6^{BTB} are stable for 36 h (500 injections) under buffer conditions of 1% or 5% DMSO. Therefore, I decided to perform screening with a 5% DMSO buffer to ensure a 1 mM solubility for the fragments.

Primary Fragment Screening.

In a primary SPR-based screening of Takeda's in-house fragment library, I was able to obtain the screening data for captured WT BCL6^{BTB}, captured MT BCL6^{BTB}, coupled WT BCL6^{BTB}, and NeutrAvidin simultaneously using the Biacore 4000 apparatus. As a result, I identified 266 fragments for captured WT BCL6^{BTB}, 256 fragments for captured MT BCL6^{BTB}, 273 fragments for coupled WT BCL6^{BTB}, and 50 fragments for NeutrAvidin (Figures 1-5A to 1-5C). The Venn diagram in Figure 1-5E summarizes the results of this fragment screening. A total of 64 compounds bind to all the BCL6^{BTB}s, hence these fragments were selected as the priority for the follow-up dose-

response tests.

Discovery and Characterization of Fragment 1.

To confirm the reproducibility and dose-responsivity of the 64 fragments, I performed dose-titration experiments. All the fragments show binding responses in a dose-dependent and reversible manner (data not shown). Next, I performed STD-NMR experiments to prioritize the 64 fragments. Seven out of the 64 fragments exhibit binding to BCL6 (data not shown). Of seven binding fragments, I focused on fragment **1** (Figure 1-6A), which shows binding to BCL6 by STD-NMR (Figure 1-6B) and furthermore competition with the BCoR peptide by SPR competition experiments (Figure 1-6C). The K_D value for **1** was determined to be 1.2 mM by SPR, and its LE was calculated to be 0.28 from its K_D value. An LE of at least 0.29 is necessary to develop an orally available candidate.[58] Therefore, **1** is a good starting point for elaboration into potent BCL6 inhibitors.

For further optimization of fragment **1**, I attempted to determine its binding mode by determining the co-crystal structure of **1** with WT $BCL6^{BTB}$. Co-crystals of **1** with $BCL6^{BTB}$ were obtained by soaking into unliganded $BCL6^{BTB}$ crystals in which the biological homodimer is related by crystallographic two-fold symmetry. Electron density indicated that **1** binds to the lateral groove at the dimer interface and exhibits alternate conformations of the aminotriazine moiety (Figures 1-7 and 1-8). The linker nitrogen forms a hydrogen bond with the main-chain oxygen of Met51. Comparison with the binding mode of 79-6 shows that **1** occupies the same site with a similar interaction pattern (data not shown). Therefore, I evaluated the BCL6 binding affinities of several pyrimidine derivatives that are structurally related to **1**.

Structure-Activity Relationships of Compounds Related to Fragment 1.

Table 1-2 summarizes the structure-activity relationships of the pyrimidine derivatives along with the original fragment **1**. Pyrimidine derivative **2** exhibits a weak binding potency (K_D = 3000 μM), while the introduction of fluorine (**3**) or chlorine (**4**) atoms onto the 5-position of compound **2** results in significantly improved binding affinities (K_D = 180 and 68 μM, respectively). Chloropyrimidine **4** exhibits good LE (0.38) and may be a promising compound for further optimization with the aim to develop more potent BCL6 inhibitors.

Structural Integration with a Second HTS hit.

Simultaneously, an independent HTS campaign for BCL6 inhibitors identified the weak BCL6 inhibitor **5** (K_D = 88 μM, LE = 0.16), which also has a pyrimidine core structure, as shown in Figure 1-5; compound **5** was discovered by the HTS campaign using the ELISA assay monitoring the interaction between the $BCL6^{BTB}$ and the BCoR peptide. The structural resemblance of **5** to **4** prompted us to integrate these two structures, forming the "hybrid compounds" shown in Figure 1-9. Co-crystal structure determination of compounds **4** and **5** with $BCL6^{BTB}$ confirmed that these compounds exhibit the same binding modes as that of the initial triazine fragment **1** (Figures 1-10 and 1-11). As expected, the two aromatic rings connected by the amine linker in the two structures significantly overlap. The co-crystal structure of **4** reveals that the chlorine atom at the 5-position of the pyrimidine core occupies a small lipophilic region of $BCL6^{BTB}$. The binding mode information on the HTS-derived pyrimidine derivative **5** shows that the carbonyl oxygen of the right-hand-side cyclic amide moiety interacts with Glu115 of $BCL6^{BTB}$. Therefore, based on the structural superposition of **5** with **4**, the hybrid compounds **6** and **7** were designed and synthesized (Table 1-3). I selected a simple unsubstituted pyridinylmethyl substituent for compound **7** while taking synthetic tractability into account.

The pyrimidine derivatives **6** and **7** exhibit significantly improved BCL6 binding affinities (K_D = 9.3 and 0.078 μM, respectively) compared to those of the fragment derivative **4** and HTS hit **5**. To confirm the binding modes, the co-crystal structures of compounds **6** and **7** were determined as well as those of the other compounds (Figures 1-12 and 1-13). The electron density map shows that the pyridine moiety of compound **7** is exposed to solvent and mostly disordered. Both compounds bind to $BCL6^{BTB}$ in the same binding mode as those for compounds **1**, **4**, and **5**. The linker nitrogen forms a hydrogen bond with the main-chain oxygen of Met51, and the carbonyl oxygen of the cyclic amide moiety interacts with Glu115. The reasons for the significant improvement in binding affinity by introduction of the pyrimidine ring are unclear because no specific structural features are observed.

As compound **7** exhibits two-digit nanomolar binding affinity along with good LE (0.37), I also evaluated the BCL6-BCoR PPI inhibitory activity of **7** in cell-free and cellular assays (Figure 1-14B to 1-14E). To evaluate the PPI inhibitory activities in cells, previously reported M2H assay was used.[13] Briefly, HEK293T cells were transfected with the GAL4-responsive reporter plasmid, the bait expression plasmid (GAL4 DNA-binding domain fused to WT BCL6, Ala5-Glu129), and the VB expression plasmid (VP16 activation domain fused to BCoR, Leu112-Ala753). Then, the PPI activities were evaluated by monitoring luciferase activities in the transfected HEK293 cell lysates. Compound **7** exhibits potent cell-free PPI inhibitory activity (ELISA IC_{50} = 0.48 μM) along with moderate cellular potency (M2H IC_{50} = 8.6 μM). Taken together, compound **7** is a promising BCL6 inhibitor candidate for further exploration.

Discussion

To find novel and promising starting points for the discovery of potent BCL6 inhibitors, I adopted an FBDD approach, which represents a challenge given that the target is a PPI. I found 64 novel binding fragments using SPR-based fragment screening, and among them, fragment **1** showed moderate LE (0.28) and competition with the BCoR peptide. Moreover, BCL6 binding affinities of several structurally related pyrimidine derivatives were also measured, and I identified the more potent fragment-like pyrimidine derivative **4** (K_D = 68 μM). Consolidation of the structural information on compound **4** with the independently obtained HTS hit **5** led to the identification of the potent BCL6 inhibitor **7** (K_D = 0.078 μM, LE = 0.37), which is >15,000-fold more potent than the initial fragment **1**. Compound **7** also exhibited an efficacy in cell-free and cellular PPI assays (ELISA IC_{50} = 480 nM, M2H IC_{50} = 8.6 μM).

$BCL6^{BTB}$ is approximately 15 kDa in size, but despite its small size, its domain contains five cysteine residues. I speculated that the high proportion of Cys residues would cause instability, which was reinforced by the fact that the co-crystal structure of $BCL6^{BTB}$ has been obtained using the Cys mutant to prevent aggregation.[37] In addition, I needed to consider that the high concentration (mM) required for SPR screening can cause false positives. In an attempt to mitigate this tendency for false positives, I decided to use the Cys-mutation protein for SPR-based screening. In the screening with the captured MT $BCL6^{BTB}$, the sensorgrams against most of the fragments show a reasonable box-shape, indicating fast binding (Figure 1-5B). Conversely, captured WT $BCL6^{BTB}$ presents many plots that indicate slow binding (Figure 1-5A). These data suggest that many fragments reversibly reacted with the Cys residues on WT BCL6 due to a concentration as high as 1 mM. Regarding the immobilization method, the binding responses of the positive control (BCoR) to coupled WT $BCL6^{BTB}$ decrease depending on the injection number, while

the binding responses of the positive control to each captured $BCL6^{BTB}$ are stable (Figures 1-5A to 1-5C). These results indicate that captured MT $BCL6^{BTB}$ is optimal for stable screening.

The total process of the fragment-based approach was summarized in Figure 1-15. Scaffold hopping of the initial triazine fragment yielded the pyrimidine fragment **2**, which enabled an introduction of a substituent occupying the small lipophilic region of $BCL6^{BTB}$. Structure-based modification of the resulting compound **4** along with the consolidation of HTS hit **5** led to the discovery of the cell-active compound **7**. The HTS hit **5** had a poor ligand efficiency (LE = 0.16), and its complex chemical structure made its modification rather difficult. Conversely, the fragment-derived compound **4** was a very good step for further modification due to its good ligand efficiency (LE = 0.38) and small molecular size. These findings suggest that the combination of biophysics-driven FBDD, SBDD, and FADD is a promising strategy for hit identification and lead generation against challenging targets such as PPIs.

Tables & Figures

Table 1-1. Binding Affinities Between BCoR Peptide and $BCL6^{BTB}$s

DMSO	WT $BCL6^{BTB}$		MT $BCL6^{BTB}$	
	K_D (μM)	R_{max} (RU)	K_D (μM)	R_{max} (RU)
1%	7.5	245	17	311
3%	9.3	242	21	302
5%	12	243	25	304

Table 1-2. Structure-Activity Relationships of the Pyrimidine Derivatives

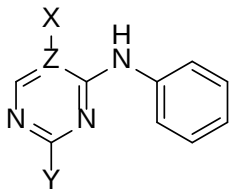

compd	X	Y	Z	K_D [a] (μM)	LE
1	-	NH_2	N	1200	0.28
2	H	NH_2	C	3000	0.25
3	F	NH_2	C	180	0.34
4	Cl	NH_2	C	68	0.38

[a] K_D values are reported as the arithmetic mean of at least two separate runs (n = 2).

Table 1-3. BCL6 Binding Affinities of the Hybrid-Type Compounds

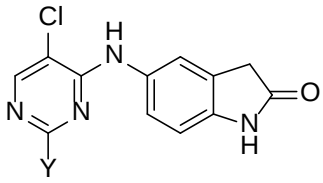

compd	Y	K_D [a] (μM)	LE
6	H	9.3	0.38
7	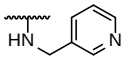	0.078	0.37

[a] K_D values are reported as the arithmetic mean of at least two separate runs (n = 2).

Table 1-4. Data collection and refinement statistics

Crystal	$BCL6^{BTB}$/**1**	$BCL6^{BTB}$/**4**	$BCL6^{BTB}$/**5**	$BCL6^{BTB}$/**6**	$BCL6^{BTB}$/**7**
Data collection					
Space group	$P6_122$	$P6_122$	$P6_122$	$P6_122$	$P6_122$
Unit cell dimensions					
a, b, c (Å)	66.4, 66.4, 152.2	66.6, 66.6, 154.6	66.4, 66.4, 152.8	66.7, 66.7, 155.3	66.9, 66.9, 153.8
α, β, γ (°)	90, 90, 120	90, 90, 120	90, 90, 120	90, 90, 120	90, 90, 120
Resolution (Å)	50–1.65 (1.68–1.65)	50–1.94 (1.97–1.94)	50–2.05 (2.09–2.05)	50–2.06 (2.10–2.06)	50–2.00 (2.03–2.00)
Observed reflections	307212	205900	87052	149914	160248
Unique reflections	24802	15813	13221	13032	14486
Redundancy	12.4 (5.4)	13.0 (8.7)	6.6 (5.3)	11.5 (8.7)	11.1 (9.4)
Completeness (%)	99.8 (96.6)	100.0 (100.0)	99.8 (100.0)	97.5 (86.0)	100.0 (100.0)
I/σ	36.2 (1.2)	37.2 (1.5)	23.9 (1.9)	28.5 (1.3)	29.0 (1.3)
R_{sym}[a]	0.057 (>1.000)	0.063 (>1.000)	0.059 (0.704)	0.069 (>1.000)	0.067 (>1.000)
Refinement					
Resolution (Å)	40–1.65 (1.69–1.65)	40–1.94 (1.99–1.94)	40–2.05 (2.10–2.05)	40–2.06 (2.12–2.06)	40–2.00 (2.05–2.00)
Reflections	23303	14958	12503	12329	13687
R_{work}[b]	0.179 (0.299)	0.188 (0.283)	0.195 (0.254)	0.193 (0.272)	0.198 (0.293)
R_{free}[b]	0.206 (0.300)	0.209 (0.303)	0.233 (0.272)	0.219 (0.374)	0.230 (0.286)
Number of atoms					
Protein	1064	1042	1042	1042	1042
Ligand/Ion	21	19	35	18	31
Water	98	40	31	25	31
Average B factor ($Å^2$)[c]	30.6	51.0	50.6	58.6	53.4
Rms deviation from ideal geometry					
Bond lengths (Å)	0.010	0.010	0.010	0.010	0.010
Bond angles (°)	1.520	1.419	1.620	1.514	1.534
Ramachandran plot (%)[d]					
Preferred regions	97.6	97.7	97.7	96.6	98.4
Allowed regions	2.4	2.3	2.3	3.9	1.6
Outliers	0.0	0.0	0.0	0.0	0.0
PDB code	**5X4M**	**5X4N**	**5X4O**	**5X4P**	**5X4Q**

[a] $R_{sym} = \Sigma_h\Sigma_i|I(h)_I - <I(h)>|/\Sigma_h\Sigma_i<I(h)>$, where <I(h)> is the mean intensity of symmetry-related reflections. [b] $R_{work} = \Sigma||F_{obs}|-|F_{calc}||/\Sigma|F_{obs}|$. R_{free} was calculated for randomly chosen 5% of reflections excluded from refinement. [c] B-factor includes contributions from TLS parameters. [d] Calculated with Coot. Values in parentheses are for the highest resolution shell.

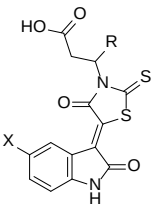

79-6: R = CO_2H, X = Br
K_D = 129 µM[a]
FX1: R = H, X = Cl
K_D = 7 µM[a]

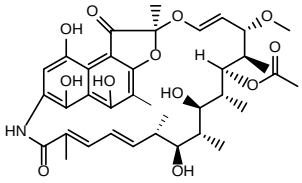

Rifamycin SV
K_D = ~ 1 mM[b]

Ac-LWYTDIRMSWRVP-OH

F1324
K_D = 0.57 nM[c]

TAT-GRGIEHISR-Fu[d]

RI-BPI
GI_{50} = ~10 µM[e]

Figure 1-1. Known BCL6 inhibitors. [a] Determined by microscale thermophoresis.[10] [b] Determined by Fluorescence polarization assay.[12] [c] Determined by SPR.[13] [d] All D-amino acids; TAT means cell penetrating peptide sequence, and Fu means fusogenic peptide sequence.[11] [e] Determined by DLBCL cell growth inhibition.[11]

(A) **(B)**

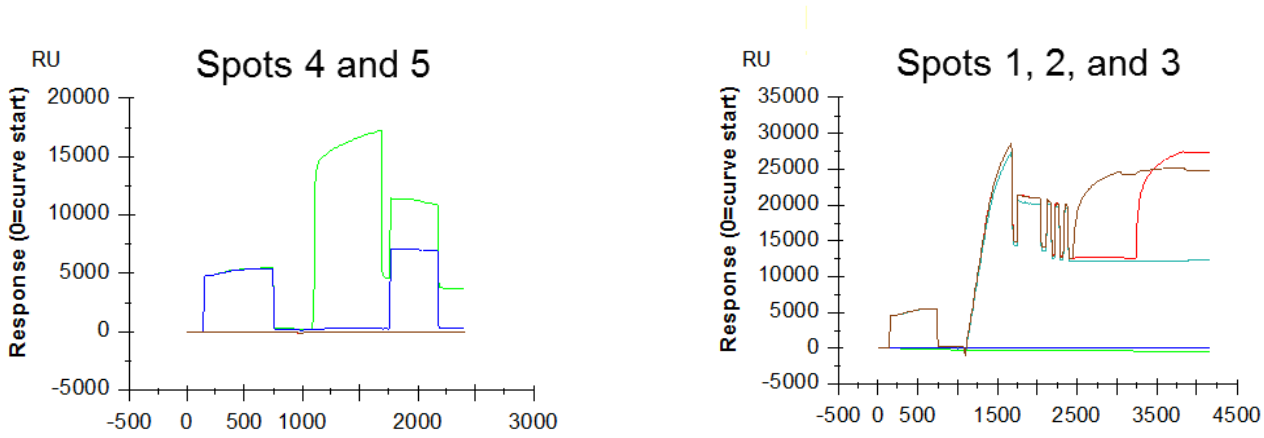

Figure 1-2. SPR sensorgrams for parallel immobilization of $BCL6^{BTB}$s. (A) WT $BCL6^{BTB}$ was immobilized on spot 5 (green) via the standard amine coupling procedure. (B) Avi-tagged WT $BCL6^{BTB}$ (brown) and avi-tagged MT $BCL6^{BTB}$ (red) were immobilized on spots 1 and 2, respectively via the SA–biotin binding.

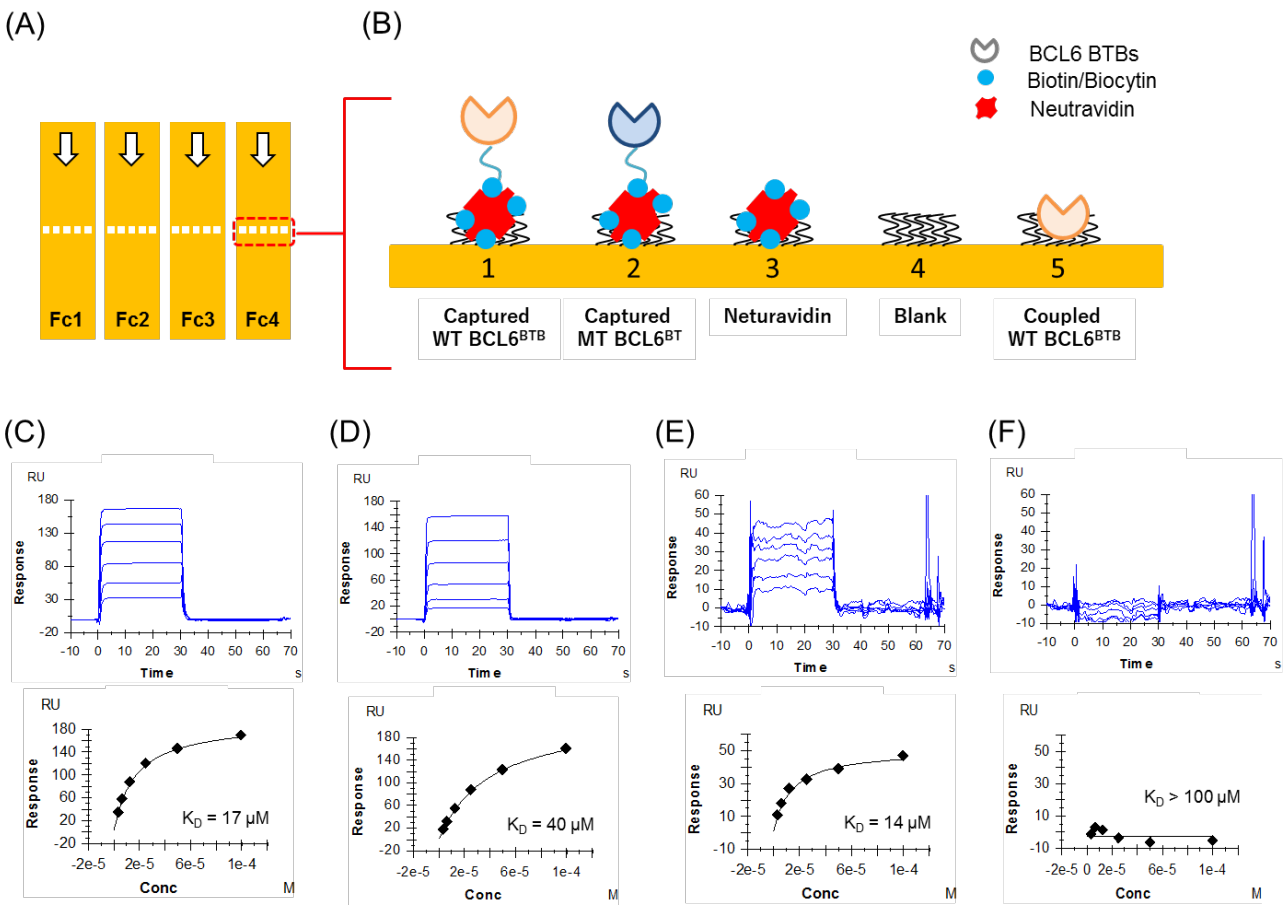

Figure 1-3. Layout of the sensor chip. (A) Four independent flow cells (Fc), each with five detection spots. (B) Protein immobilized in each flow cell. Binding responses of captured WT BCL6^{BTB}, captured MT BCL6^{BTB}, coupled WT BCL6^{BTB}, and NeutrAvidin are detected on spots 1–3, spots 2–3, spots 5–4, and spots 3–4, respectively. Sensorgrams of BCoR peptide binding to (C) captured WT BCL6^{BTB}, (D) captured MT BCL6^{BTB}, (E) coupled WT BCL6^{BTB}, and (F) NeutrAvidin. Lower graphs indicate the fit plots of the response measured at equilibrium plotted against BCoR peptide concentration. Top concentration is 100 µM; dilution step is 2-fold.

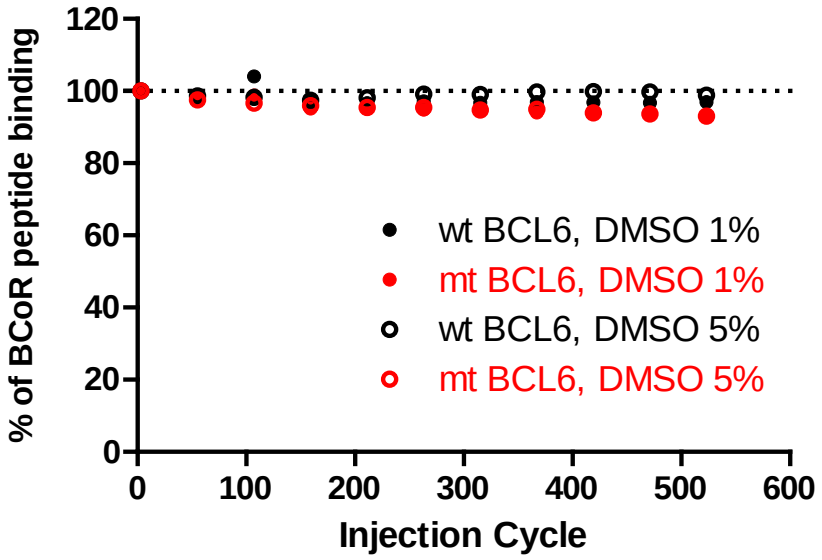

Figure 1-4. Evaluation of stability and DMSO effect. For every 52nd cycle, the BCoR peptide was injected at 50 µM over each captured $BCL6^{BTB}$.

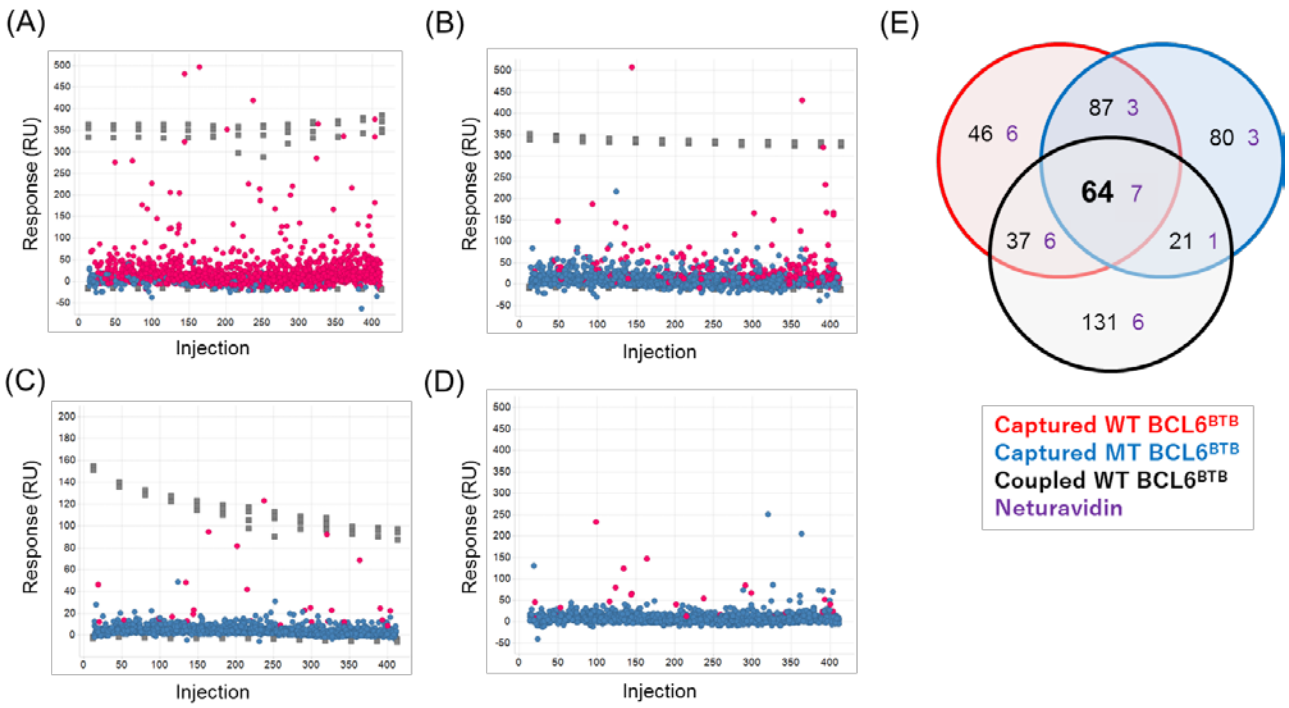

Figure 1-5. SPR-based screening of 1494 fragments tested against (A) captured WT BCL6^{BTB}, (B) captured MT BCL6^{BTB}, (C) coupled WT BCL6^{BTB}, and (D) NeutrAvidin. The color of each plot indicates fast binding (blue-circle), slow binding (red-circle), and 100 μM BCoR peptide as a positive control (gray-square). (E) Venn diagram showing the number of fragments selected at each BCL6^{BTB} screening and the overlap of fragments found by each screening.

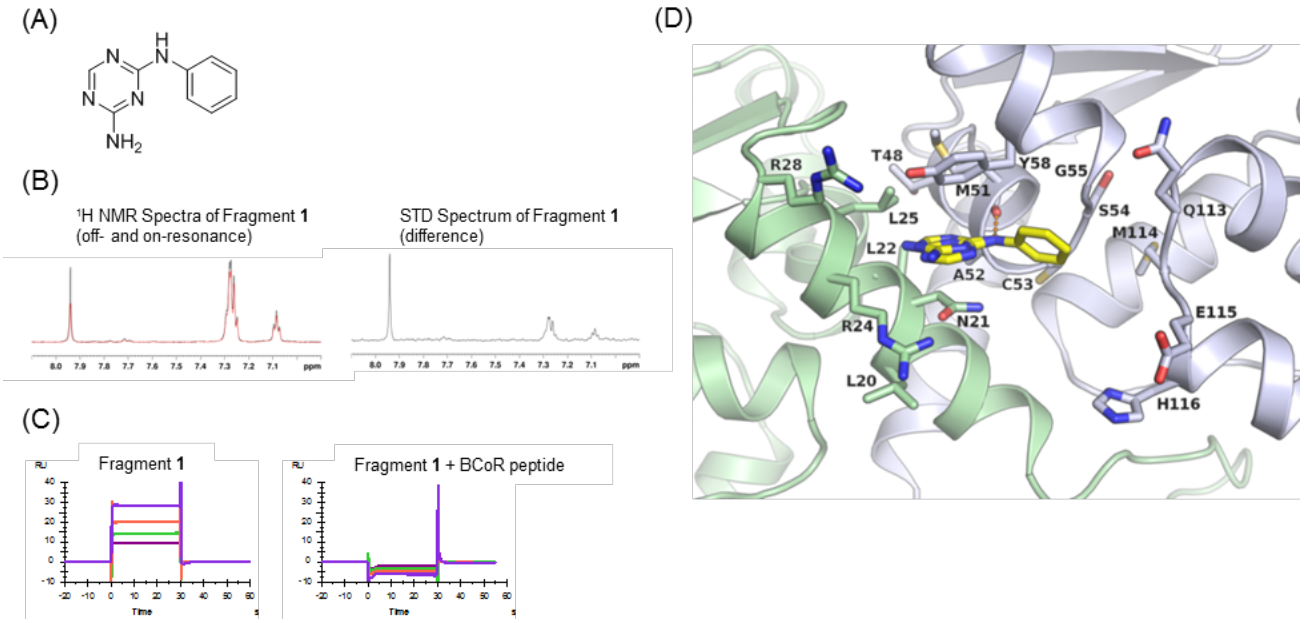

Figure 1-6. Characterization of fragment **1**. (A) Chemical structure of fragment **1**. (B) STD-NMR experiments. ^{1}H spectra of fragment **1** for off-resonance (black line) and on-resonance (red line), and the STD spectrum of fragment **1** (difference). (C) SPR competition experiments. Sensorgrams of fragment **1** to MT BCL6^{BTB} in the absence or presence of 100 µM BCoR peptide. Top concentration is 1 mM; dilution step is 2-fold. (D) Co-crystal structure of fragment **1** in complex with BCL6^{BTB}.

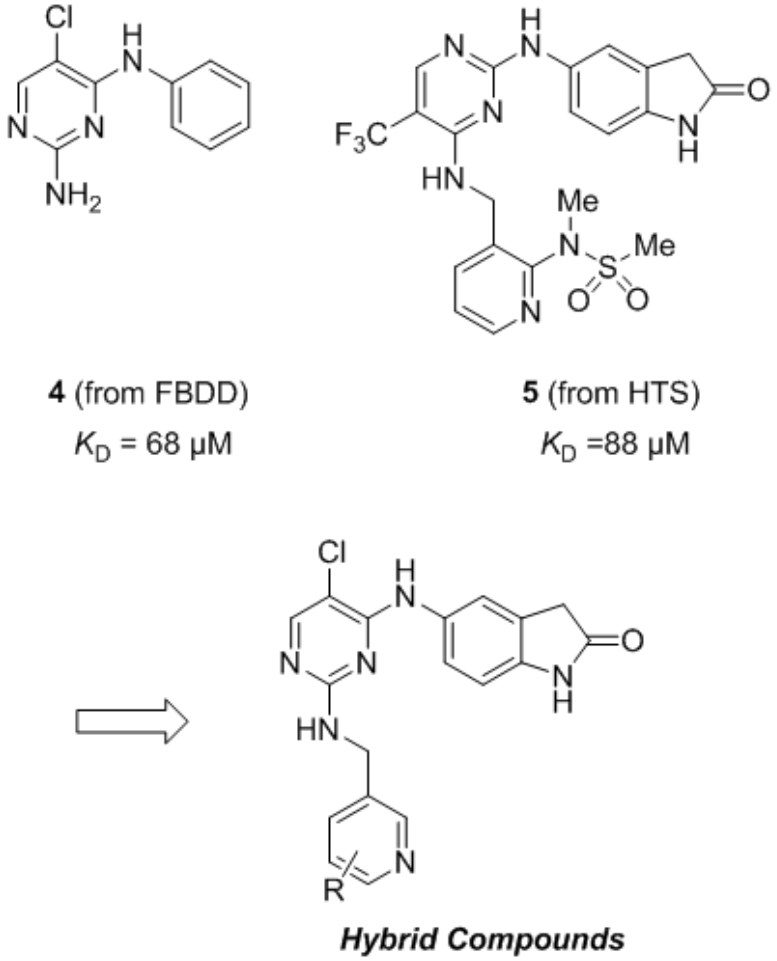

Figure 1-7. Consolidation of the fragment-based inhibitor **4** with hit compound **5**.

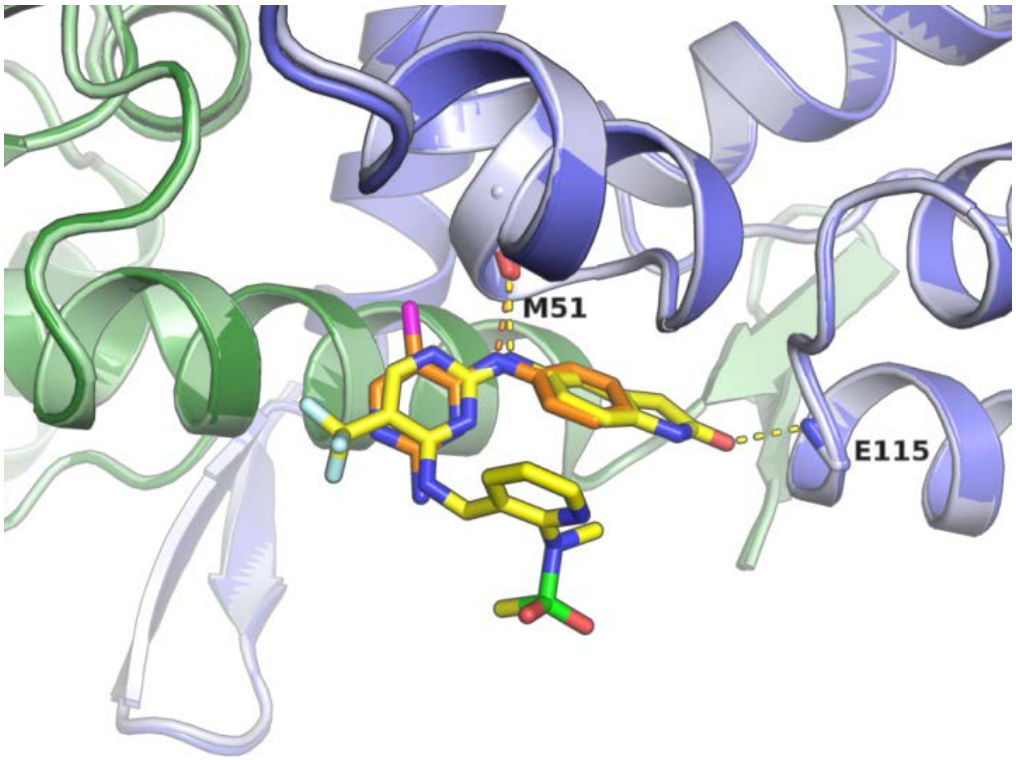

Figure 1-8. Structural superposition of the complex structures with compounds **4** (orange) and **5** (yellow).

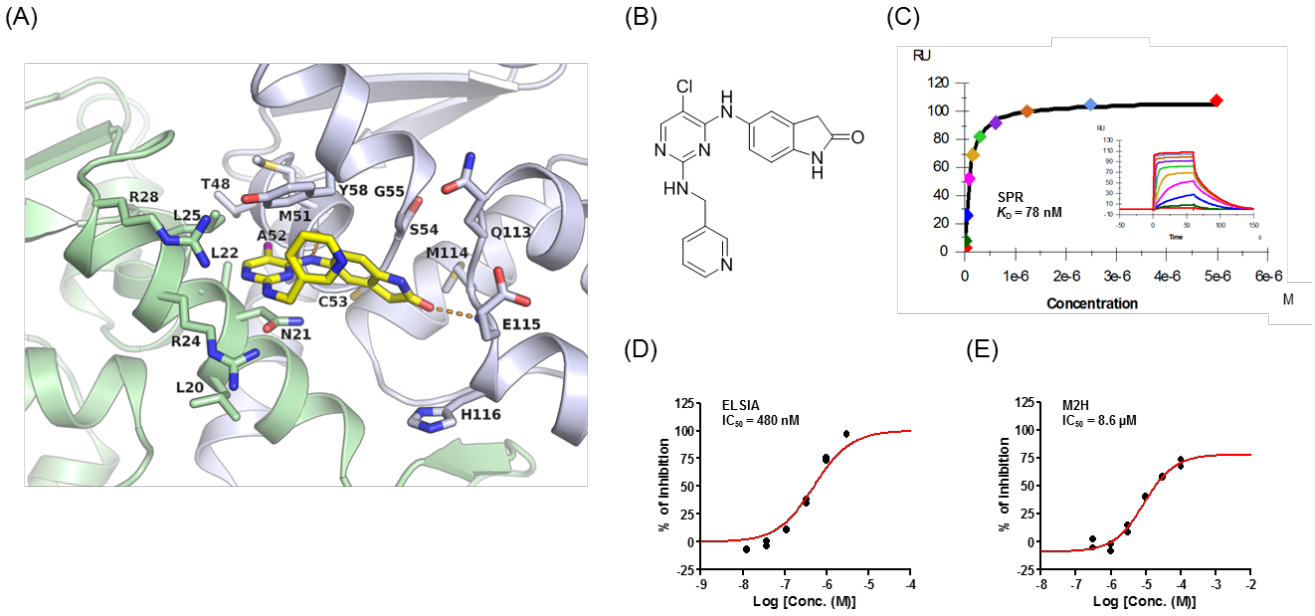

Figure 1-9. (A) Co-crystal structure of compound **7** in complex with $BCL6^{BTB}$. (B) Chemical structure of **7**. (C) Equilibrium plot and sensorgrams (insert) of **7** binding to BCL6. (D, E) PPI inhibitory activities in cell-free (ELISA) and cellular (M2H) assays.

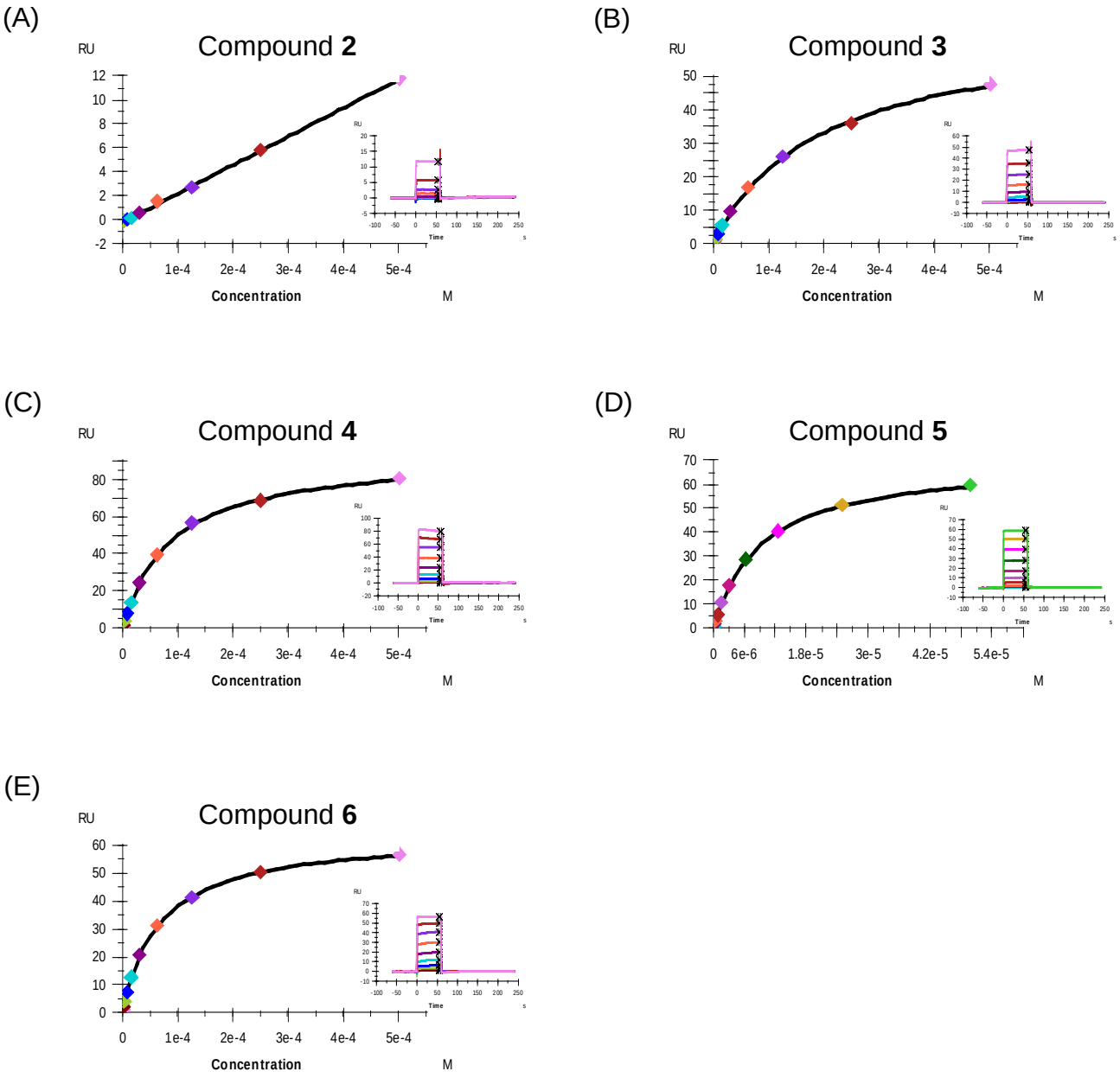

Figure 1-10. SPR sensorgrams (insert) and equilibrium plots for compounds **2**–**6**. Top concentration is 50 μM; dilution step is 2-fold.

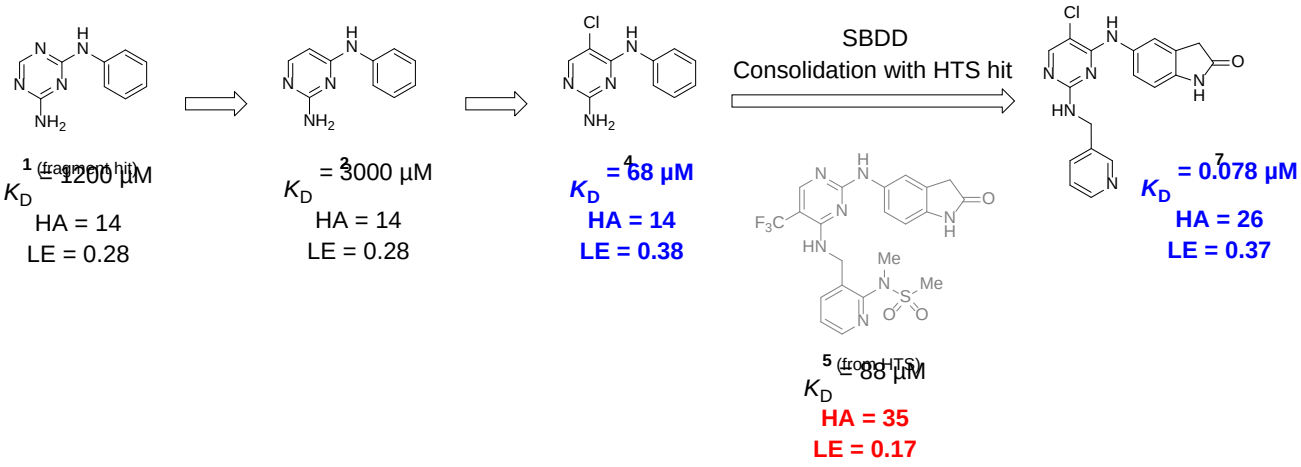

Figure 1-11. Summary of the FBDD approach for identification of the compound **7**.

(A)

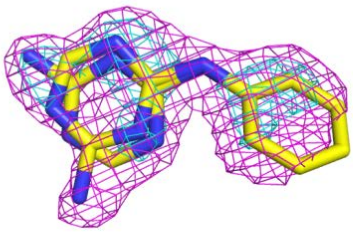

(B)

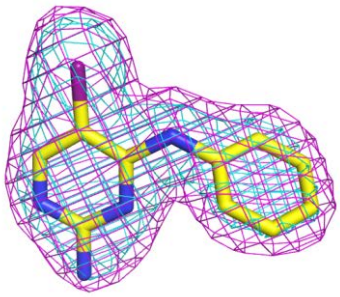

(C)

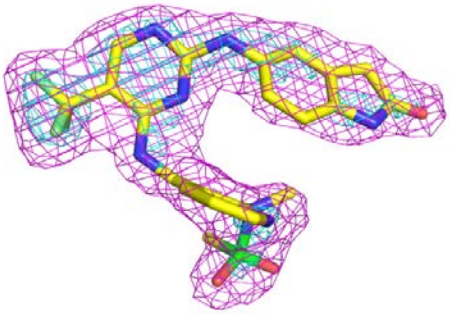

(D)

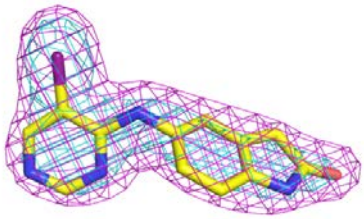

(E)

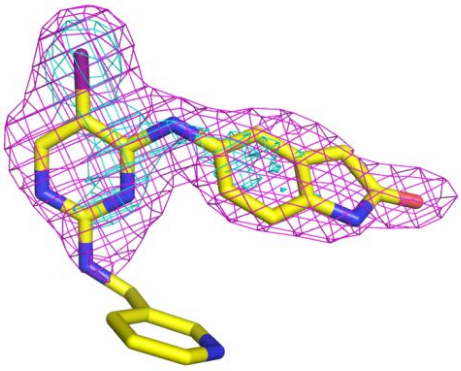

Figure 1-12. F_{obs}–F_{calc} electron density omit maps contoured at 3σ (magenta) and 6σ (cyan) for the vicinity of the compounds. (A) compound **1**, (B) compound **4**, (C) compound **5**, (D) compound **6**, and (E) compound **7**.

Chapter II:

Discover of K-Ras(G12D)-Selective Inhibitory Peptide by Random Peptide T7 Phage Display Technology and Its Structural Characterization

Abstract

Amino-acid mutations of Gly^{12} (*e.g.* G12D, G12V, G12C) of V-Ki-ras2 Kirsten rat sarcoma viral oncogene homolog (K-Ras), the most promising drug target in cancer therapy, are major growth drivers in various cancers. Although over 30 years have passed since the discovery of these mutations in most cancer patients, effective mutated K-Ras inhibitors have not been marketed.

Here, I report novel and selective inhibitory peptides to K-Ras(G12D). I screened random peptide libraries displayed on T7 phage against purified recombinant K-Ras(G12D), with thorough subtraction of phages bound to wild-type K-Ras, and obtained KRpep-2 (Ac-RRCPLYISYDPVCRR-NH_2) as a consensus sequence. KRpep-2 showed more than 10-fold binding- and inhibition-selectivity to K-Ras(G12D), both in SPR analysis and GDP/GTP exchange enzyme assay. K_D and IC_{50} values were 51 and 8.9 nM, respectively. After subsequent sequence optimization, I successfully generated KRpep-2d (Ac-RRRRCPLYISYDPVCRRRR-NH_2) whose K_D and IC_{50} values were 8.9 and 1.6 nM, respectively and significantly suppressed ERK-phosphorylation, downstream of K-Ras(G12D), along with A427 cancer cell proliferation at 30 μM peptide concentration. Furthermore, the crystal structure of the human K-Ras(G12D) mutant was determined in complex with GDP and KRpep-2d at 1.25 Å resolution. This structure revealed that the peptide binds near Switch II and allosterically blocks protein–protein interactions with the guanine nucleotide exchange factor. This discovery of a unique binding pocket provides valuable information that will facilitate the design of direct Ras inhibitors. To my knowledge, this is the first report of a K-Ras(G12D)-selective inhibitor, contributing to the development and study of K-Ras(G12D)-targeting drugs.

Introduction

Somatic mutations in small GTPase Ras drive neoplasia in various cancers. The K-Ras isoform is most frequently mutated in 86% of Ras-driven cancers [59], with 83% of K-Ras amino-acid mutations at residue Gly^{12} where G12D is the major substitution.[60] Therefore, development of anti-cancer drugs targeting mutated K-Ras will benefit several patients.

Despite being a promising drug target for cancer therapeutics, effective drugs targeting mutated K-Ras have not been marketed.[61] K-Ras remains a challenging target, and the generation of direct inhibitors remains difficult, because the K-Ras molecular surface is round and has less druggable pockets for conventional small molecules; furthermore, no allosteric regulatory sites have been reported to date.[62] Moreover, K-Ras changes its structure in the presence/absence of GDP or GTP, and binding affinities between K-Ras and GDP/GTP are too strong (picomolar affinity) to be inhibited by small molecules.[63]

In this context, some direct K-Ras inhibitors, based on novel approaches, were reported, such as covalent inhibitors or peptide inhibitors.[64] The former strategy involves an irreversible binding to Cys^{12} of K-Ras(G12C). For example, Ostrem *et al.* screened 480 disulfide-fragment compounds by protein mass spectrometry and identified several fragments that react with the G12C mutant but not with the wild-type (WT) K-Ras, in the presence of GDP.[65] The latter strategy involves using a peptide alternative to small molecule compounds. Patgiri *et al.* extracted a K-Ras-binding sequence from son of sevenless 1 (SOS1), which catalyzes the transition of K-Ras/GDP (inactive-form) to K-Ras/GTP (active-form), and stabilizes its alpha-helix structure through a hydrocarbo-staple method to inhibit protein-protein interactions (PPI) between K-Ras and SOS proteins.[66] The SAH-SOS1 peptide bound to both WT K-

Ras and mutants with equal affinity, and the binding activity was not dependent on the presence of GDP or GTP. Instead of using natural protein sequences, Pei *et al.* identified artificial cyclic peptide inhibitors from a random peptide displayed beads library.[67-69] They prepared recombinant K-Ras(G12V) as a fusion protein with GST, and introduced a chemical label to GST *via* fluorescent dye Texas Red on a Lys. By using this fluorescent labeled K-Ras mutant, 6×10^6 various cyclic peptides were screened, and sequences binding K-Ras with submicromolar affinity were identified.

These approaches successfully generated K-Ras inhibitors. However, Cys-reactive small molecules present concerns regarding undesirable side effects due to their potential for promiscuous inhibition. Moreover, the aforementioned peptide inhibitors did not display sufficient inhibition activities and showed poor selectivity toward mutated K-Ras. In this study, I focused on K-Ras(G12D) as the target molecule, since G12D is the most common substitution in many K-Ras-driven cancers and the side-chain structure/size of Asp has greater potential for selectivity compared to other substitutions such as Cys (G12C) or Val (G12V). I screened random peptide libraries displayed on T7 phage against recombinant K-Ras(G12D) in GDP states. By using phage display, I can screen 10^{11} distinct clones, which is much greater than that included in Pei *et al.*'s aforementioned peptide beads library. Furthermore, I thoroughly subtracted phages bound to WT K-Ras in the phage panning process. As a result, I successfully discovered K-Ras(G12D)-selective inhibitory peptides. Here, I demonstrate the notable selectivity and inhibition activities of the peptides to K-Ras(G12D) through cell-free and cell-based assays. For further characterization, I performed structural determination of K-Ras(G12D) in complex with GDP and KRpep-2d, which allowed an investigation of the protein binding site and peptide binding conformation. This structural analysis indicated a unique binding site for

small molecules, and it might therefore provide a valuable basis for the future design of K-Ras inhibitors.

Materials & Methods

Preparation of recombinant K-Ras proteins.

Human KRAS(Met1–Lys169) (NCBI Reference Sequence: NM_004985) DNA sequence was isolated from human cDNA clone (GeneCopoeia, Rockville, MD) and was ligated into a pET21a vector (Merck Millipore, Darmstadt, Germany) with a C-terminus His-Avi-tag. Expression plasmids were co-transfected with the BirA expression plasmid, which is constructed internally and encodes a biotin protein ligase, into *E. coli* BL21(DE3) (Nippon Gene, Toyama, Japan). Protein expression was induced with 0.1 mM IPTG, followed by addition of 50 μM D-biotin and culture for 16 h at 16°C. Cells were harvested by centrifugation, suspended in lysis buffer (50 mM Tris (pH 8.0), 1 mM DTT, 150 mM NaCl, 5 U/mL Nuclease), and centrifuged at 15000 × g for 20 min. The proteins were purified by NiNTA superflow column (QIAGEN, Hilden, Germany) and HiLoad 26/60 Superdex 200 pg column (GE Healthcare, Piscataway, NJ).

Phage library construction and panning.

T7 phage libraries displaying random peptides, which were generated by mixed-oligonucleotides as template DNA, were constructed by using T7Select 10-3 vector from Merck Millipore, according to methods described previously[70-71] . Biotinylated Avi-tagged K-Ras protein was preincubated with 1 mM GDP in reaction buffer (0.5% BSA, 10 mM $MgCl_2$ in PBS) at 4°C overnight to prepare the GDP-form, and then immobilized onto Dynabeads M280 SA (Invitrogen, Carlsbad, CA). After washing the beads by PBS containing 0.1% Tween20 (PBST), the beads

were incubated with phage libraries for 1 h with 1 mM GDP and 50 μg/mL non-tagged WT K-Ras in reaction buffer, and subsequently washed with PBST. The bound phages were eluted with 1% SDS and transfected into *E. coli* BLT5615 cells (Merck Millipore) in log-phase growth for phage amplification. After bacteriolysis, phages were recovered from the culture supernatant by centrifugation and PEG-precipitation, dissolved in PBS, and used for the next round of panning.

Peptide synthesis.

Peptide synthesis was conducted using Fmoc-chemistry on a Symphony X peptide synthesizer (Protein Technologies, Inc., Tucson, AZ, USA). The resin for peptide synthesis and Nα-Fmoc (and side chain) protected amino acids were purchased from Novabiochem-Merck Millipore (Darmstadt, Germany) and Watanabe Chemical Industries, Ltd. (Hiroshima, Japan). The following side-chain protections were used: Arg(Pbf), Asp(OtBu), Cys(Trt), Ser(tBu) and Tyr(tBu). Solvents and other reagents were reagent-grade and were used further purification unless otherwise noted. N,N'-Diisopropylcarbodiimide (DIPCDI), OxymaPure, and TFA were purchased from Wako Pure Chemical Industries, Ltd. (Osaka, Japan). Piperidine was purchased from Watanabe Chemical Industries. Crude peptides were purified to homogeneity by reverse phase (RP)-HPLC with the following conditions: YMC-Actus Triart Prep C8-S S-10 μm 20 nm column (30 × 250 mm); solvent gradient A, 0.1% TFA in water; B, 0.1% TFA in acetonitrile with gradient indicated below; flow rate, 15 mL/min; and UV detector, 220 nm. The purity of the products was characterized by analytical HPLC. Reverse phase analyzes were performed using a Shimazu gradient system with a YMC Triart C8 column (4.6 × 100 mm). The peptide molecular weights were confirmed by matrix-assisted laser desorption ionization−time of flight (MALDI−TOF) MS on a Bruker Autoflex Speed system (Bruker Daltonics,

Kanagawa, Japan).

Sieber amide resin (0.71 mmol/g, 140.8 mg, 0.1 mmol) was swelled with NMP. Sequential peptide chain elongation via Fmoc/OxymaPure®/DIPCDI (6 eq. of reagents) chemistry was performed in NMP, followed by N-terminal acetylation and vacuum drying on a Symphony X peptide synthesizer to yield the desired peptide resin: Ac-Arg(Pbf)-Arg(Pbf)-Arg(Pbf)-Arg(Pbf)-Cys(Trt)-Pro-Leu-Tyr(tBu)-Ile-Ser(tBu)-Tyr(tBu)-Asp(OtBu)-Pro-Val-Cys(Trt)-Arg(Pbf)-Arg(Pbf)-Arg(Pbf)-Arg(Pbf)-NH-Sieber amide resin (762 mg). The dried resin was suspended in 7 mL of TFA/m-cresol/thioanisole/H_2O/triisopropylsilane/ethandithiol (80:5:5:5:2.5:2.5) and stirred for 180 min at room temperature. Diethyl ether was added to the reaction solution, after which the precipitate was centrifuged and the supernatant was removed. After repeating this washing procedure, the residue was extracted with an aqueous acetic acid solution and filtered to remove the resin. The filtrate was applied to preparative HPLC with a linear density gradient elution (60 min) was performed using eluent A/B ratios of 77/23−67/33 (eluent A: 0.1% TFA in water and eluent B: 0.1% TFA-containing acetonitrile) on a YMC-Actus Triart Prep C8-S S-10 μm 20 nm column (30 × 250 mm) with a flow rate of 15 mL/min. The product-containing fractions were collected and lyophilized to yield 100.4 mg of the desired peptide, Ac-Arg-Arg-Arg-Arg-Cys-Pro-Leu-Tyr-Ile-Ser-Tyr-Asp-Pro-Val-Cys-Arg-Arg-Arg-Arg-NH2, as a white powder with a mass spectrum of (M + H) + 2562.41 (calc. 2562.40). The RP-HPLC elution time was 6.89 min, and the elution conditions were as follows: YMC Triart C8 column (4.6 × 100 mm), linear density gradient elution with eluent A/B ratios of 80/20−30/70 (25 min; eluent A: 0.1% TFA in water and eluent B: 0.1% TFA-containing acetonitrile), and a flow rate of 1 mL/min.

Ac-Arg-Arg-Arg-Arg-Cys-Pro-Leu-Tyr-Ile-Ser-Tyr-Asp-Pro-Val-Cys-Arg-Arg-Arg-Arg-NH2 (5 mg) was

dissolved in 1.0 mol/L Tris-HCl buffer (pH 8.5, 4 mL) and acetonitrile (2 mL). DMSO (2 mL) was added to this solution, which was stirred for 36 h at room temperature. The solution was then filtered and applied to the preparative HPLC column, and a linear density gradient elution (60 min) was performed with eluent A/B ratios of 75/25−65/35 (eluent A: 0.1% TFA in water and eluent B: 0.1% TFA-containing acetonitrile) on a YMC-Actus Triart Prep C8-S S-10 μm 20 nm column (30 × 250 mm) at a flow rate of 15 mL/min. The product-containing fractions were collected and lyophilized to yield 3.1 mg of the desired KRpep-2d peptide, Ac-Arg-Arg-Arg-Arg-Cys(&)-Pro-Leu-Tyr-Ile-Ser-Tyr-Asp-Pro-Val-Cys(&)-Arg-Arg-Arg-Arg-NH2 (disulfide), as a white powder with a mass spectrum of (M + H) + 2560.66 (calc. 2560.38). The elution time on RP-HPLC was 8.00 min, and the elution conditions were as follows: YMC Triart C8 column (4.6 × 100 mm), linear density gradient elution with eluent A/B ratios of 80/20−30/70 (25 min; eluent A: 0.1% TFA in water and eluent B: 0.1% TFA-containing acetonitrile), and a flow rate of 1 mL/min.

Peptide binding evaluation by SPR.

SPR biosensing experiments were performed on Biacore3000 and BiacoreS200 equipped with Sensorchip SA at 25°C (GE Healthcare).

For immobilization, HBS-P+ (10 mM Hepes, 150 mM NaCl, 0.05% surfactant P20, pH 7.4, GE Healthcare) was used as the running buffer. Apo-, GDP-, and GTP-form K-Ras were prepared by pretreatment with 5 mM EDTA, 1 mM GDP, or 1 mM GTP, respectively. For immobilization, each biotin-K-Ras was injected over the sensorchip surface. Typical immobilization levels were around 5000 RUs.

For the interaction study, HBS-P+ supplemented with 1% DMSO and with/without 10 μM GDP or GTP was used as a running buffer. Peptides diluted in series were injected at a flow rate of 50 μL/min for 120 s, and the

dissociation was thereafter followed for up to 240 s. Data processing and analysis were performed by Biaevaluation software ver. 4.1.1 and BiacoreS200 evaluation software (GE Healthcare). Sensorgrams were double-referenced prior to global fitting the concentration series to 1:1 binding with the mass-transport model. Dissociation constant K_D was calculated from the following equation $K_D = k_{off}/k_{on}$.

Competition experiments were performed by sequential injection of peptide solutions either individually, or as mixtures of two peptides, each for 120 s at a flow rate of 50 μL/min. When peptides occupied different sites, the response observed for the mixture was the sum of the 2 individual responses observed for the peptides.

In vitro enzyme assay.

BODIPY-FL-GDP, Terbium-labeled SA (Tb-SA), and human SOS1 protein (Exchange Domain 564-1049) were purchased from Life Technologies (Carlsbad, CA), Cisbio (Codolet, France), and Cytoskeleton (Denver, CO), respectively.

TR-FRET assay was carried out using 384-well plates (784075, Greiner Bio-One, Frickenhausen, Germany) and the signal was measured using an EnVision plate reader (PerkinElmer, Waltham, MA). The solution in each well was excited with a laser (λ=337 nm) reflected by a dichroic mirror (D400/D505), and fluorescence from Tb and BODIPY were detected through two emission filters (CFP 486 nm for Tb, Emission 515 nm for BODIPY). Biotin-K-Ras mutants (WT, G12C, and G12D) were diluted to 2 μM in EDTA buffer (20 mM HEPES, 50 mM NaCl, 10 mM EDTA, and 0.01% (w/v) Tween20) and preincubated for 30–60 min at room temperature. The EDTA pretreated K-Ras proteins were diluted to 3 nM in Ras assay buffer (20 mM HEPES, 50 mM NaCl, 10 mM $MgCl_2$, 0.01% (w/v) Tween20) containing 0.5 nM Tb-SA and 30 nM BODIPY-GDP and further incubated for over 6 h at room temperature.

Various concentrations of 45 nL peptides (100-fold concentration) in DMSO were dispensed in each well of the assay plate using Access Echo555 (Labsite, Sunnyvale, CA). Next, 1.5 μL of Ras assay buffer with/without 3 mM DTT was dispensed into each well. The plate was sealed with a plate sealer and incubated for over 1 h. Subsequently, 1.5 μL of K-Ras/Tb-SA/BODIPY-GDP premix was added to the assay plate and the TR-FRET signal was measured with the plate reader to obtain TR-FRET signal at t = 0. GDP-GTP exchange reaction was initiated by addition of 1.5 μL of Ras assay buffer containing 30 μM GTP and 150 nM SOS1 protein, and TR-FRET signal was measured at an arbitrary time. Final concentrations of K-Ras protein, Tb-SA, BODIPY-GDP, SOS1, GTP, and DTT were 1 nM, 0.17 nM, 10 nM, 50 nM, 10 μM, and 1 mM, respectively.

To obtain the GDP-GTP exchange rate (k_{obs}) for 0% inhibition, time course of TR-FRET signal was fitted with equation (1).

$$\text{TR}-\text{FRET signal} = (Y_0 - Y_\infty)\exp(-k_{\text{obs}}t) + Y_\infty \quad (1)$$

where Y0 and $Y\infty$ represent the TR-FRET signal at initial and completion of the reaction, respectively. The k_{obs} of 100% inhibition was determined by TR-FRET signal change in the absence of SOS1 protein. TR-FRET signal was fitted with equation (1) by fixing the $Y\infty$ value to that obtained by 0% inhibition. k_{obs} values at each concentration of peptides were obtained by using the same fitting procedure as for 100% inhibition. The inhibition rate of K-Ras activity was calculated according to equation (2).

$$\text{Inhibition rate}\,(\%) = 100 \times \left(\frac{k_{\text{H}} - k_{\text{obs}}}{k_{\text{H}} - k_{\text{L}}} \right) \quad (2)$$

where k_H and k_L are k_{obs} of the 0% and 100% inhibition, respectively. The dose-response data were then fitted to a logistic curve using GraphPad Prism 5 (GraphPad Software, San Diego, CA) to determine IC_{50} values.

In vitro cell-based assays.

For western blot, cells were seeded at 5×10^4 cells/well into 24-well plates, and were serum-starved for 16 h on the following day. Cells were treated with the peptides diluted in FBS-free medium for 30 min, followed by treatment with peptides in FBS-containing medium for 1 h, washed briefly with ice-cold saline, and scraped in SDS sample buffer (Wako Pure Chemical Industries, Ltd., Osaka, Japan). Proteins were separated by 7.5–15% gradient SDS polyacrylamide gel electrophoresis (Perfect NT gel, DRC) and were electrophoretically transferred onto a nitrocellulose membrane. The membranes were blocked in StartingBlock T20 (PBS) Blocking Buffer (Thermo Fisher Scientific Inc., MA, USA), and labeled with a primary anti-pERK1/2 antibody (Cell Signaling Technology, #9101), and an anti-ERK1/2 antibody (Cell Signaling Technology, #9102), both diluted in Can Get Signal Solution I (Toyobo, Osaka, Japan), at 4°C overnight. The labeled membrane was washed with PBST and incubated for 30 min with a secondary antibody linked to horseradish peroxidase diluted in Can Get Signal Solution II (Toyobo). The protein bands were visualized using an ImmunoStar LD (Wako) with a bioimaging analyzer LAS3000 (GE Healthcare), and quantified using ImageQuant TL (GE Healthcare).

For the growth inhibition assay, A427 and A549 cells were seeded at 4000 and 2000 cells/well in 96-well plates, respectively. Cells were treated with the peptides on the following day. For the 3-day treatments, medium containing the peptides was replaced every day. Relative cell numbers were estimated using CellTiter-Glo (Promega, Madison, WI) according to the manufacturer's instructions. Luminescence was measured using an EnVision plate reader. Percent inhibition was calculated based on cell numbers at Day 0 as low control and at Day 3 without peptide as high control.

X-ray crystallography.

The complex of K-Ras(G12D) with GDP and KRpep-2d was prepared by incubating 3-fold molar excesses of ligands on ice for 2–3 h prior to the crystallization experiments. The complex was crystallized from a reservoir solution containing 0.1 M Hepes (pH 7.5) and 50% (v/v) PEG 200 at 20°C via the sitting-drop vapor diffusion method. Prior to data collection, crystals were immersed in reservoir solution containing 30% ethylene glycol as a cryoprotectant and flash-frozen in liquid nitrogen. Diffraction data were collected from a single crystal using the DECTRIS Pilatus3-S6M PAD detector (Baden-Daettwil, Switzerland) with a BL-17A beamline (Photon Factory, Tsukuba, Japan) under a 100-K nitrogen cryostream. The diffraction data were reduced and scaled using HKL2000.[72] The structure was solved according to the molecular replacement method using Phaser [73] from the CCP4 software suite [74] and the K-Ras structure (PDB code 4QL3) as a search model. Refinement was performed using REFMAC5 [49] and individual isotropic restrained B factors. Progress was monitored using R_{free}, and 5% of the data were set aside for cross-validation before refinement. For TLS refinement, the protein and ligands were set as a single rigid body.[50] Interactive model building was performed using COOT, [75] and the final models were validated using Molprobity.[51] All graphical figures were generated using PyMOL (Schrödinger LLC, Cambridge, MA, USA). A schematic diagram of protein–ligand interactions was generated using LIGPLOT.[76]

Results

Identification of K-Ras(G12D)-binding sequences by phage display screening.

To obtain K-Ras(G12D)-binding peptide sequences, random peptide libraries displayed on T7 phage were

screened against recombinant biotin-K-Ras(G12D) immobilized onto SA magnetic beads in the presence of 1 mM GDP, 10 mM Mg^{2+} ion, and 50 μg/mL non-tagged WT K-Ras. After subsequent phage cloning, binding screening, and DNA sequencing of phages, two major clusters possessing Y/W-M/L-C-Y/F/W-P-M/L/I/Y-K/R/V/A-L/M-X-X-X-C or R/K-C-P/M/L/I/V-L/I/M-Y/F/K/R-I/V/T/L/S-S/T/R/K-X-D-P/K/R-V/M/L-C, and one minor cluster possessing C-M/R-W-W-R-E-I/V-C-P-V/E-W/T-W were found. Three consensus sequences: KRpep-1 (Ac-PPWYMCYPMKLKPDC-OH), -2 (Ac-RRCPLYISYDPVCRR-NH_2), and -3 (Ac-CMWWREICPVWW-OH) were chemically synthesized (Table 2-1).

Binding analysis and characterization of synthetic peptides by SPR.

To determine binding kinetics of peptides, an evaluation system using SPR was constructed. First, the interactions between K-Ras and SOS1 proteins were evaluated to confirm immobilized Ras protein activity. Interestingly, the SOS1 protein bound to the GDP-form more strongly than to the apo-form of K-Ras (results from representative G12D-mutant are shown in Figure. 2-1A). Furthermore, the SOS1 protein was released from K-Ras by addition of free GTP in solution. These data suggest that the GDP-form of K-Ras is selectively recognized by the SOS1 protein and K-Ras function is allosterically controlled by the SOS1 protein and GTP abundance.

Next, I evaluated the binding activities of peptides to K-Ras proteins. Remarkably, KRpep-2 presented K_D value of 51 nM to K-Ras(G12D) with 9-fold selectivity to G12C K-Ras and 14-fold selectivity to WT K-Ras (Figure. 2-1B, Table 2-1, and 2-2). In contrast, KRpep-3 exhibited K_D value of 65 nM to K-Ras(G12D), but displayed a reduced binding selectivity (Table 2-1, Figure. 2-2, and Table 2-2). KRpep-1, that belongs to the other major cluster, showed weak binding affinities (>μmol range) (Table 2-1). Interestingly, KRpep-2 and -3 bound to the GDP-/GTP-

forms but not to the apo-form of K-Ras proteins (Figure. 2-3).

To characterize the binding of KRpep-2 and -3, a competition experiment was performed using SPR. In this evaluation, after injecting solutions of each peptide at a single concentration (>90% occupancy), a mixture of two peptides was subsequently injected. When peptides occupied different sites, the response observed for the mixture was the sum of the 2 individual responses observed for the peptides.[77] As shown in Figure 2-1C, the response observed for the KRpep-2/-3 mixture was similar to the signal of each peptide alone, predicting that KRpep-2 and -3 bind in a similar fashion or possess overlapped binding sites on K-Ras(G12D).

Since KRpep-2 exhibited K-Ras(G12D) selectivity and a stronger binding activity than that of KRpep-3, I focused on KRpep-2 and evaluated its binding capacity in competition against the SOS1 protein. The binding activity of the SOS1 protein to K-Ras(G12D) in the presence of KRpep-2 was monitored through SPR. As a result, the binding response was significantly decreased (Figure 2-1D). However, the negative control peptide did not show such an effect. These results indicate that KRpep-2 and SOS1 protein could have overlapped binding sites on K-Ras(G12D).

Peptide sequence optimization by KRpep-2-derived phage library.

For affinity enhancement, a KRpep-2-derived T7 phage library (XXRRCPLYISYDPVCXXXX, X = random amino acid residues, under line = 20% expression of indicated amino acids) was constructed and re-screened against K-Ras(G12D) with stricter panning conditions than those applied to the first one. As a result, KRpep-2d (Ac-RRRRCPLYISYDPVCRRRR-NH_2) was found as the consensus sequence. Namely, there is no sequence changes except for an additional Arg extension at the N- and C-termini. The K_D value of KRpep-2d was determined to be 8.9 nM to the GDP-form of K-Ras by using SPR (Table. 2-3).

Enzyme inhibition activities of synthetic peptides.

The SOS1 protein interacts with the GDP-form of K-Ras and mediates the GDP-GTP exchange reaction on the K-Ras protein leading to the GTP-form of K-Ras.[66] Therefore, I evaluated the inhibition activities of KRpep-2 and KRpep-2d against the exchange reaction of BODIPY-GDP to GTP on K-Ras proteins by TR-FRET (Figure 2-4A). As a result, both peptides inhibited the exchange reaction in a peptide concentration-dependent manner, with G12D-mutant selectivity against other K-Ras variants (WT and G12C) (Figure 2-4B and Table 2-4). The IC_{50} values were estimated at 8.9 nM and 1.6 nM, respectively. However, their inhibition activities were decreased in reducing conditions, suggesting that the disulfide bond was cleaved and the peptides could not retain their constrained cyclic structure (Figure 2- 4B and Table 2-4).

To examine peptide-cyclization by non-disulfide-bonds, I tested *o*-xylene-cyclization, which proved to be effective as an alternative to disulfide bond cyclization in the previous study.[27] However, it significantly reduced the K-Ras inhibitory activity (Table 3, KRpep-2(ox)). One possible reason is that *o*-xylene-cyclization provides a larger cyclic form of peptide, and the difference in ring size might influence its binding activity. Furthermore, the bulkier structure of *o*-xylene, compared to that of a disulfide bond, might disturb the binding to K-Ras.

K-Ras(G12D)-selective inhibition of peptides in cell-based assays.

To evaluate the cellular K-Ras inhibitory activity and selectivity of the synthetic peptides (KRpep-2d and KRpep-2dL (negative control)), I investigated the effects of the peptides on the phosphorylation levels of ERK1/2, which is a downstream signal of K-Ras, in A427 (lung, G12D mutant) and A549 (lung, G12C mutant) cells. In these cells, K-Ras-dependent phosphorylation of ERK has been reported.[78] Western blot analysis revealed that KRpep-2d

selectively inhibited the phosphorylation levels of ERK1/2 in A427 cells at a peptide concentration of 30 μM (Figure 2-5A). Furthermore, KRpep-2d significantly suppressed cell proliferation of A427 cells but not that of A549 cells at a peptide concentration of 30 μM (Figure 2-5B), suggesting that this growth inhibitory activity was not caused by non-specific cytotoxicity of the peptide. In contrast, KRpep-2dL did not inhibit the ERK signal or cell proliferation at 30 μM. Collectively, these results suggest that KRpep-2d entered cells, bound to intracellular K-Ras(G12D), and inhibited the signaling cascade.

Determination of the crystal structure of K-Ras(G12D) in complex with GDP and KRpep-2d.

The crystal structure of K-Ras in complex with GDP and KRpep-2d was determined at 1.25 Å resolution. The crystallographic processing and refinement statistics are summarized in Table 2-5. One molecule was included per asymmetric unit. Except for two N-terminal residues derived from the expression tag, the K-Ras(G12D) polypeptide chain is sufficiently well-ordered to allow structural feature interpretation. The crystal structure revealed that KRpep-2d binds near Switch II and the α3 helix in an extended and shallow cleft composed of two α-helices (Figure 2-6). The main-chain atoms of KRpep-2d were well-ordered in crystal packing, although the electron densities of the side-chain atoms of N- and C-terminal arginine residues (Arg1–Arg4 and Arg16–Arg19) were relatively ambiguous (Figure 2-7). Four arginine residues at each terminus were exposed to solvent, and therefore, they did not interact specifically with K-Ras, except for crystal-packing interactions (Figure 8A). Notably, the inhibitory activity (IC_{50}) and binding affinity (K_D) of KRpep-2d were approximately 5-fold stronger than those of KRpep-2 (Ac-RRCPLYISYDPVCRR-NH_2), a lead peptide of KRpep-2d (Table 2-1 to 2-4). It was suggested that these arginine residues at both termini participate in indirect KRpep-2 interactions. The crystal structure showed that KRpep-2d has

an intramolecular hydrogen bond between the acetyl oxygen of the N-terminus and the main-chain nitrogen of Arg19 of the C-terminus (Figure 2-8A). Along with the intramolecular disulfide bond, the hydrogen bond between terminal residues might contribute to stabilizing the overall peptide conformation to adopt favorable direct interactions with K-Ras.

The loop conformation of KRpep-2d results from the formation of an intramolecular disulfide bond between Cys5 and Cys15. Both hydrophilic and hydrophobic interactions were observed at the binding interface between KRpep-2d and K-Ras(G12D) (Figures 2-8A and 2-8B). The main-chain nitrogen and oxygen of Leu7 form hydrogen bonds with the side-chain oxygen and nitrogen of Gln99 in the α3 helix, respectively. The main-chain nitrogen and oxygen of Tyr8 form hydrogen bonds with the main-chain oxygen of Gln61 and the side-chain nitrogen of Arg68 in the α2 helix. The main-chain nitrogen and side-chain oxygen of Ser10 interact via hydrogen bonding with the side-chain oxygens of Asp69 in the α2 helix. The side chain of Pro6 interacts hydrophobically with the side chain of Tyr96 in the α3 helix. The side chain of Leu7 occupies a small hydrophobic pocket involving Val9, Thr58, Arg68, Met72, and Tyr96. The side chain of Ile9 interacts hydrophobically with the side chain of Met72 in the α2 helix. The side chain of Tyr11 forms a water-mediated hydrogen bond with the main-chain oxygen of Val103 in the α3 helix. The side chain of Asp12 forms hydrogen bonds with the side-chain nitrogens of Gln99 and Arg102 in the α3 helix. The side chain of Val14 interacts via van der Waals stacking with the side chain of Arg102. Together, these results indicate that the conformation of KRpep-2d, when anchored by the intramolecular disulfide bond, is optimal for interaction with the shallow and extended cleft of K-Ras. Alanine scanning of KRpep-2d prior to the structural analysis revealed that Leu7, Ile9, and Asp12 are especially critical for the inhibition of K-Ras(G12D). [79] SPR binding analysis also

demonstrated that replacement of Leu7, Ile9, and Asp12 with alanine significantly attenuated the peptide binding affinity for K-Ras (Table 2-6). The structural information regarding the binding interaction is highly consistent with the structure-and-activity relationships.

Discussion

Herein, I produced the first K-Ras(G12D)-selective binding/inhibitory peptides designed from random peptide T7 phage display technology. Especially, KRpep-2d presented a remarkable selectivity toward K-Ras(G12D), not only in cell-free enzyme assay, but also in cell-based assays. My peptides recognized a single point mutation of Gly^{12} on K-Ras that may cause subtle differences in the protein structure.[80] Furthermore, KRpep-2 bound to GDP-/GTP-forms of K-Ras(G12D) while it did not bind to its Apo-form, indicating that the binding site is not the GDP/GTP binding site, an undruggable pocket. The binding competition assay revealed that the main mechanism involves the inhibition of PPI between K-Ras(G12D) and the SOS1 protein. Binding affinity and selectivity characteristics are possible through the capacity of a peptide to form an ideal shape against the target surface and interact with it by multi-point binding.

Patgiri *et al.* and Pei *et al.* reported K-Ras inhibitory peptides obtained by *de novo* design or screening peptide library on beads, respectively.[66-69] However, these do not have K-Ras mutant-selectivity. I could discover KRpep-2 because the diversity of the screening library. My library contains a hundred billion distinct clones possessing different ring size peptides. Furthermore, I performed a thorough subtraction of WT K-Ras-binding phages. Although KRpep-1 and -3, for which the K-Ras(G12D)-selectivity was low, were isolated, the subtraction would lead to an

enrichment of KRpep-2 related peptide sequences in the phage panning process. Therefore, display technology represented by phage display is an extremely powerful strategy to generate molecules possessing high-affinity and -selectivity.

To evaluate structural rearrangement of K-Ras, the K-Ras(G12D)–GDP–KRpep-2d complex structure was compared with the active GTP-bound and inactive GDP-bound K-Ras(G12D) structures, as guanine nucleotide exchange was reported to induce large conformational changes in the Switch I and Switch II regions. The structural comparison revealed that the Switch II region resembles the GDP-bound state (Figure 9A). In the K-Ras(G12D)–GDP and K-Ras(G12D)–GDP–KRpep-2d complexes, the side chain of Asp12 formed a direct or water-mediated hydrogen bond with Gln61 of Switch II, whereas in the K-Ras(G12D)–GMPPCP and K-Ras(G12D)–GMPPNP complexes, the side chain of Gln61 was exposed to solvent, resulting in a loss of interaction with the side chain of Asp12 (Figures 2-9B and 2-9C). In the K-Ras(G12D)–GTP analog complexes, the α2 helix of Switch II overlapped with the KRpep-2d binding site. Although the Switch II conformation significantly differs between the GDP- and GTP-bound states, the binding affinity of KRpep-2d for both states is approximately equivalent (Table 2-3). The increased structural flexibility of Switch II in the GTP-bound state may be tolerable to KRpep-2d binding.

Intriguingly, KRpep-2d exhibits inhibitory selectivity against K-Ras(G12D) compared with the G12C mutant and WT for both states. To understand the specificity, my ternary K-Ras(G12D) complex was compared with the K-Ras(G12C)–GDP and K-Ras(WT)–GDP complexes. The Switch II conformation in the K-Ras(WT)–GDP complex is similar to that of K-Ras(G12D) in the GDP state (Figure 10A), whereas the Switch II conformation in the K-Ras(G12C)–GDP complex is similar to that of K-Ras(G12D) in the GTP state (Figure 2-10B). Despite of the

structural differences of Switch II between K-Ras(WT) and K-Ras(G12C), the binding affinity of KRpep-2d for both K-Ras proteins is relatively weak in comparison with that for K-Ras(G12D) to the same extent. Structural comparison indicated that a hydrogen-bonding interaction between Asp12 and Gln61 likely stabilizes the Switch II conformation for peptide binding. As a result, the stabilized conformation of Switch II may facilitate the binding capability of KRpep-2d.

To explore the inhibitory mechanism of KRpep-2d, my structure was compared with the Ras–GEF complex. GEFs such as SOS1 catalyze the release of GDP and permit the binding of GTP. Therefore, Ras–GEF inhibition could feasibly decrease the proportion of GTP-bound Ras. An SPR binding competition assay demonstrated that KRpep-2 competes for binding to SOS1, and indicated that KRpep-2 and SOS1 could share binding sites on K-Ras(G12D). The αH helix within the helical hairpin motif of SOS1 is known to play an important role in the nucleotide-exchange mechanism.[81] Structural comparison with the H-Ras–SOS1 complex showed that the binding site of KRpep-2d is distal to the binding region of the αH helix of SOS, which displaces Switch I and Switch II to mediate GDP release (Figure 2-11). KRpep-2d binding stabilized the Switch II conformation and caused steric hindrances with the SOS1 αH helix, suggesting that KRpep-2d is likely a non-orthosteric inhibitor of the nucleotide-exchange reaction that interferes allosterically with nucleotide binding or release. Although the helical hairpin of SOS1 is critical for its function, other regions of the catalytic cdc25 domain of SOS1 also interact with Ras.[82-83] As the binding site of KRpep-2d is adjacent to the αB, αD, and αK helices of the cdc25 domain, the inhibitory mechanism of KRpep-2d remains controversial (Figure 2-12).

The PPIs between Ras–GTP and its effectors, which initiate various downstream signaling cascades, are also challenging targets. Structural information may facilitate a detailed understanding of the binding capabilities of inhibitors. KRpep-2d also binds to the GTP-bound state of K-Ras with comparable affinity (K_D = 11 nM; Table 2-3). It remains to be determined whether KRpep-2d inhibits Ras–effector interactions. One orthosteric inhibitor of Ras–effector interactions, Kobe2061,[84] is known to bind to a similar site adjacent to Switch II as compound **13** (Figure 2-13A), indicating the importance of the Switch II conformation for Ras-effector binding.[85] According to one plausible hypothesis, KRpep-2d could prevent Switch I and Switch II from adopting the correct conformations for Raf-RBD binding (Figure 2-13B). However, preliminary analysis of K-Ras(G12D) binding with Raf-RBD is still under investigation. Further investigation may facilitate an understanding of the mechanism of action of KRpep-2d.

Here, fortunately, KRpep-2d had consecutive Arg residues in the N-/C-termini, resulting in an effective cell penetration activity of the peptide, as shown in the previous study.[27] As expected, KRpep-2d (30 μM) inhibited the downstream signal of K-Ras (ERK-phosphorylation) and suppressed A427 cell proliferation with K-Ras(G12D)-selectivity. Nevertheless, its efficacy was not sufficient for *in vivo* experiments. KRpep-2d possesses the hydrophilic residue Ser^{10} and acidic residue Asp^{12} in its sequence, and these residues may decrease the cell-membrane permeability of the peptide. To increase cell penetration activity, I examined palmitoylation of the N-terminus of KRpep-2d, since a combination of oligo-Arg and hydrocarbon moieties enhances cellular membrane affinity and subsequent cell-internalization ability.[86] However, C16-KRpep-2d showed non-specific binding and strong cytotoxicity in preliminary experiments (data not shown). A combination with drug delivery systems such as liposomes or nanoparticles may be effective to deliver KRpep-2d into cells.

In addition to cell-membrane permeability, disulfide bond cyclization is another disadvantage of KRpep-2d, since the inhibition activity was decreased in reducing conditions (Figure 2-4B). Unfortunately, *o*-xylene bridging caused a loss in K-Ras inhibitory activity. I need to assess other bridging modifications such as carba [87] and lactam [88] bridging pathways, that would provide resistance to reducing conditions and thereby, retain the inhibition activity of KRpep-2d, even in cytosolic reducing conditions.

As described above, the characteristics of KRpep-2d can still be improved. Nevertheless, it represents the first K-Ras(G12D)-selective inhibitor to date, whose inhibition activity and selectivity were demonstrated in both cell-free and cell-based assays; KRpep-2d will mark a new chapter in the study of K-Ras direct inhibitors.

Tables & Figures

Table 2-1. Sequences and K_D values of peptides.

Peptide	Sequence	K_D (nM)					
		GDP-form			GTP-form		
		G12D	G12C	WT	G12D	G12C	WT
KRpep-1	Ac-PPWYMCYPMKLKPDC-OH	1000	2300	17000	1400	2000	2500
KRpep-2	Ac-RRCPLYISYDPVCRR-NH_2	51	480	700	100	920	1300
KRpep-3	Ac-CMWWREICPVWW-OH	65	210	77	93	350	220

WT means wild type.

Table 2-2. Binding kinetic parameters of KRpep-2 and -3.

Peptide	K-Ras	Ligand	K_D (nM)	k_{on} ($M^{-1}s^{-1}$)	k_{off} (s^{-1})	Chi^2 (RU^2)	Binding $t_{1/2}$ (s)
KRpep-2	G12D	GDP	8.9	1.3×10^6	1.1×10^{-2}	2.52	61
	G12C		35	1.0×10^6	3.5×10^{-2}	3.21	20
	WT		58	1.6×10^6	9.3×10^{-2}	1.39	7.5
	G12D	GTP	11	2.8×10^6	3.0×10^{-2}	9.95	23
	G12C		250	3.7×10^5	9.2×10^{-2}	7.29	7.5
	WT		200	6.1×10^5	1.2×10^{-1}	1.93	5.8
KRpep-3	G12D	GDP	8.9	1.3×10^6	1.1×10^{-2}	2.52	61
	G12C		35	1.0×10^6	3.5×10^{-2}	3.21	20
	WT		58	1.6×10^6	9.3×10^{-2}	1.39	7.5
	G12D	GTP	11	2.8×10^6	3.0×10^{-2}	9.95	23
	G12C		250	3.7×10^5	9.2×10^{-2}	7.29	7.5
	WT		200	6.1×10^5	1.2×10^{-1}	1.93	5.8

WT means wild type.

Table 2-3. Kinetic parameters of KRpep-2d binding.

Peptide	K-Ras	Ligand	K_D (nM)	k_{on} ($M^{-1}s^{-1}$)	k_{off} (s^{-1})	Chi^2 (RU^2)	Binding $t_{1/2}$ (s)
KRpep-2d	G12D	GDP	8.9	1.3×10^6	1.1×10^{-2}	2.52	61
	G12C		35	1.0×10^6	3.5×10^{-2}	3.21	20
	WT		58	1.6×10^6	9.3×10^{-2}	1.39	7.5
	G12D	GTP	11	2.8×10^6	3.0×10^{-2}	9.95	23
	G12C		250	3.7×10^5	9.2×10^{-2}	7.29	7.5
	WT		200	6.1×10^5	1.2×10^{-1}	1.93	5.8

WT, wild-type; $t_{1/2}$, half-life

Table 2-4. Inhibition activities of peptides assessed through enzyme assay.

				IC_{50} (nM) (-/+ DTT)		
Name	Sequence	Cyclization	Structure	G12D	G12C	WT
KRpep-2	Ac-RR-Cys-PLYISYDPV-Cys-RR-NH_2	Disulfide	-S-S-	8.9 / 1500	130	170
KRpep-2d	Ac-RRRR-Cys-PLYISYDPV-Cys-RRRR-NH_2	Disulfide	-S-S-	1.6 / 87	18	42
KRpep-2d(ox)	Ac-RRRR-Cys-PLYISYDPV-Cys-RRRR-NH_2	*o*-xylene	-S  S-	2600 / 1200	25000	31000
KRpep-2dL	Ac-RRRR-Nle-PLYISYDPV-Nle-RRRR-NH_2	None (linear)		N.D. / N.D.	N.D.	N.D.

N.D. means not determine

Table 2-5. Data Collection and Refinement Statistics.

Crystal	K-Ras(G12D)−GDP−KRpep-2d
Data collection	
Space group	$P3_121$
Unit cell dimensions	
a, b, c (Å)	51.5, 51.5, 129.6
α, β, γ (°)	90, 90, 120
Resolution (Å)	50−1.25 (1.27−1.25)
Unique reflections	56366 (2780)
Redundancy	9.3 (7.3)
Completeness (%)	100.0 (99.7)
I/σ	54.4 (1.9)
R_{sym} [a]	0.041 (0.964)
Molecules in ASU	1
Refinement	
Resolution (Å)	45−1.25 (1.28−1.25)
Reflections	53531 (3866)
R_{work} [b]	0.171 (0.273)
R_{free} [b]	0.194 (0.293)
Number of atoms	
Protein	1431
Ligand/Ion	211
Water	138
Average B factor (Å^2) [c]	19.1
Rms deviation from ideal geometry	
Bond lengths (Å)	0.011
Bond angles (°)	1.592
Ramachandran plot (%) [d]	
Preferred regions	97.7
Allowed regions	2.3
Outliers	0.0
PDB code	**5XCO**

[a] $R_{sym}=\Sigma_h\Sigma_i|I(h)_i-<I(h)>|/\Sigma_h\Sigma_i<I(h)>$, where <I(h)> is the mean intensity of symmetry-related reflections. [b] $R_{work}=\Sigma||Fobs|-|F_{calc}||/\Sigma|F_{obs}|$. R_{free} was calculated for randomly chosen 5% of reflections excluded from refinement. [c] B-factor includes contributions from TLS parameters. [d] Calculated with Coot. Values in parentheses are those for the highest resolution shell.

Table 2-6. Binding Affinities of KRpep-2d and Amino-acid Substituted Derivatives.

Modification from KRpep-2d	K_D (nM)					
	K-Ras−GDP			K-Ras−GTP		
	G12D	G12C	WT	G12D	G12C	WT
(KRpep-2d)	8.9	35	58	11	250	200
$Arg^{1,2,18,19}$ → deletion (KRpep-2)	51	480	700	100	920	1300
$Arg^{1,2,3,4,16,17,18,19}$ → deletion	770	680	> 1000	> 1000	> 1000	> 1000
$Arg^{1,19}$ → D-Arg	10	290	140	11	560	260
Pro^{6} → Ala	55	520	560	260	> 1000	> 1000
Leu^{7} → Ala	920	> 1000	> 1000	> 1000	> 1000	> 1000
Tyr^{8} → Ala	89	740	910	190	> 1000	> 1000
Ile^{9} → Ala	> 1000	> 1000	> 1000	> 1000	> 1000	> 1000
Ser^{10} → Ala	78	570	990	160	> 1000	> 1000
Tyr^{11} → Ala	220	> 1000	> 1000	470	> 1000	> 1000
Asp^{12} → Ala	> 1000	> 1000	> 1000	> 1000	> 1000	> 1000
Pro^{13} → Ala	26	170	320	33	750	670
Val^{14} → Ala	8.9	38	83	9.9	240	210

(A)

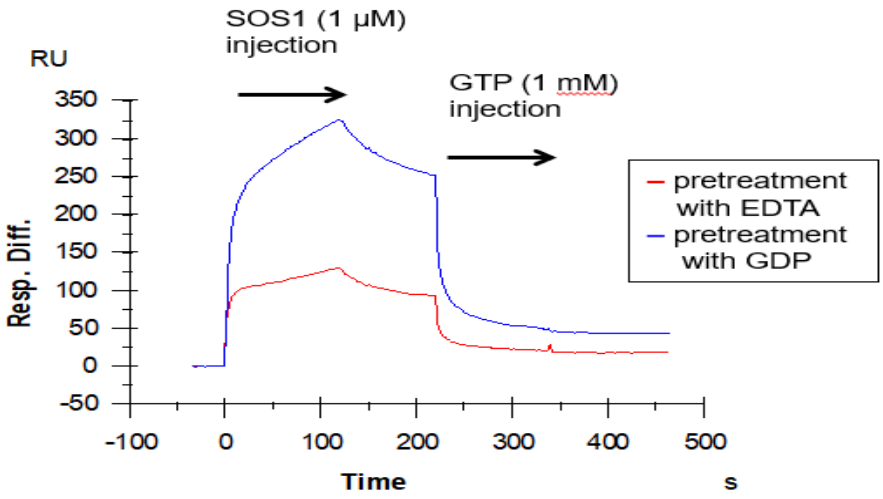
SOS1 (1 μM)
injection
RU
GTP (1 mM)
injection
pretreatment
with EDTA
pretreatment
with GDP
Resp. Diff.
350
300
250
200
150
100
50
0
-50
-100
0
100
200
300
400
500
Time
s

(B)

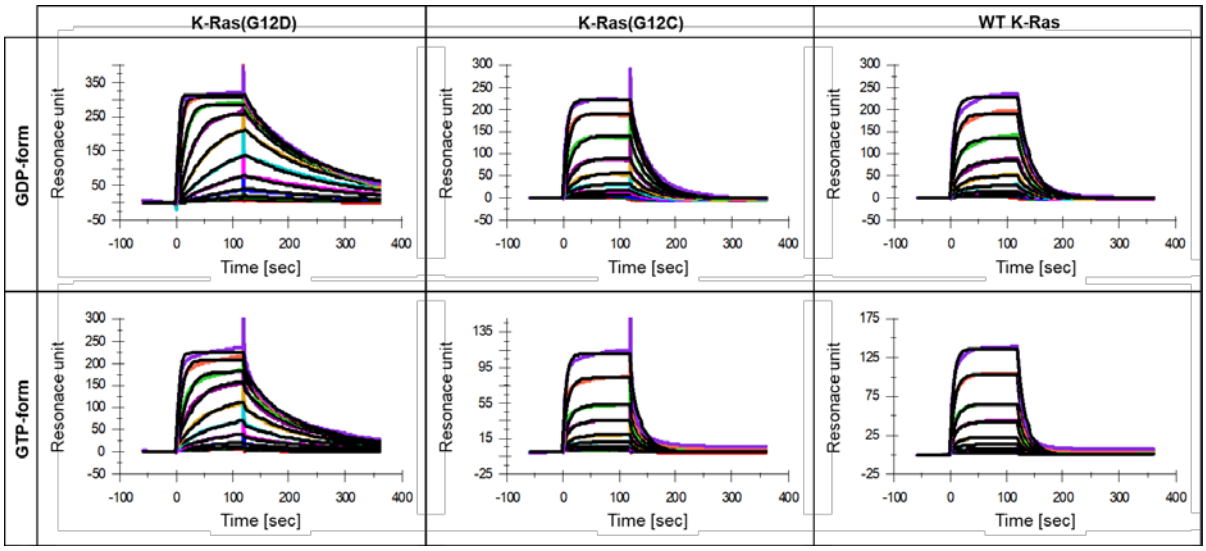
K-Ras(G12D)
K-Ras(G12C)
WT K-Ras
GDP-form
GTP-form
Resonace unit
Time [sec]

(C)

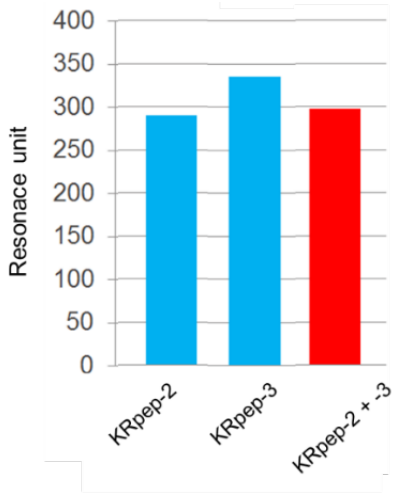

(D)

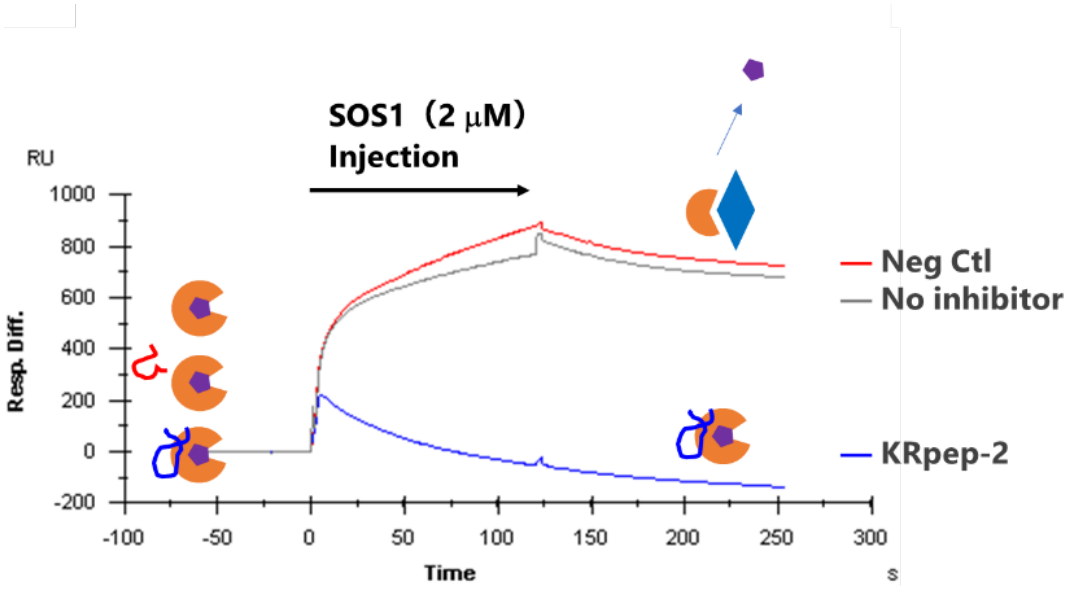

Figure 2-1. Binding activity of peptides toward each K-Ras protein determined through SPR. (A) Binding activities of SOS1 to Apo- or GDP-form of K-Ras(G12D). (B) Binding activities of KRpep-2. The colored and black solid lines indicate the experimental (from top 2 μM, 2-fold dilution) and fitting (1:1 binding model) data, respectively. (C) Competition experiments between KRpep-2 (2 μM) and -3 (2 μM) that occupy overlapped binding sites on K-Ras(G12D). (D) Binding competition between KRpep-2 and SOS1 on K-Ras(G12D) protein. SOS1 was injected in K-Ras(G12D)-immobilized cell in the presence or absence of peptide.

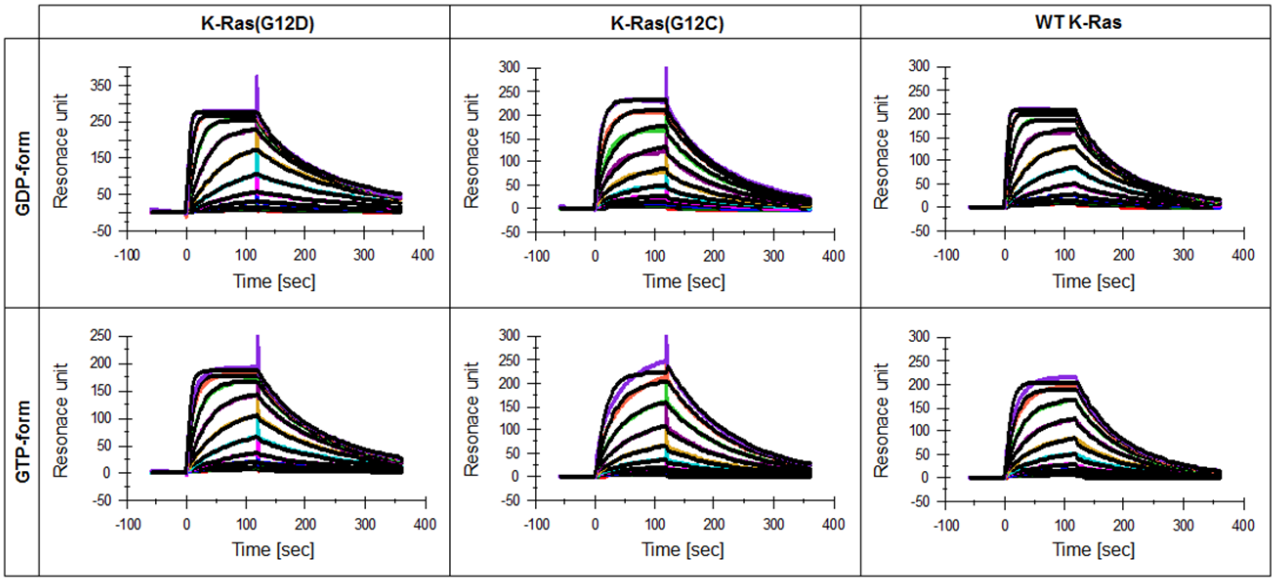

Figure 2-2. Binding activity and selectivity of KRpep-3 determined through SPR. The colored and black solid lines indicate the experimental (from top 2 μM, 2-fold dilution) and fitting (1:1 binding model) data, respectively.

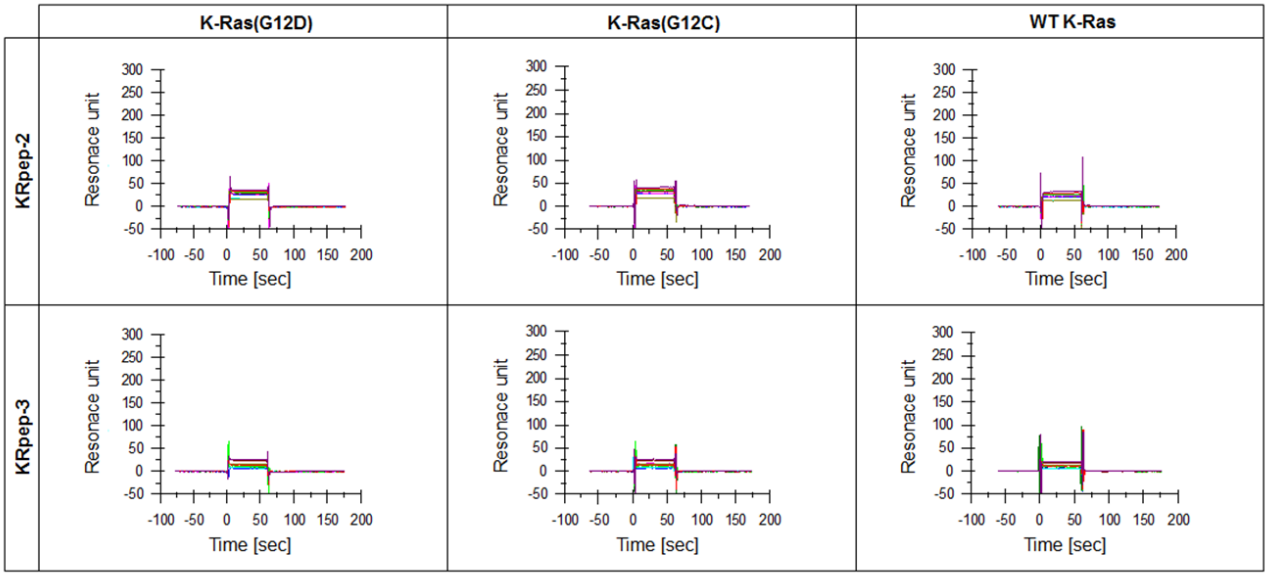

Figure 2-3. Binding activities of KRpep-2 and -3 toward apo-form K-Ras proteins. The colored indicates the experimental (from top 2 μM, 2-fold dilution) data.

(A)

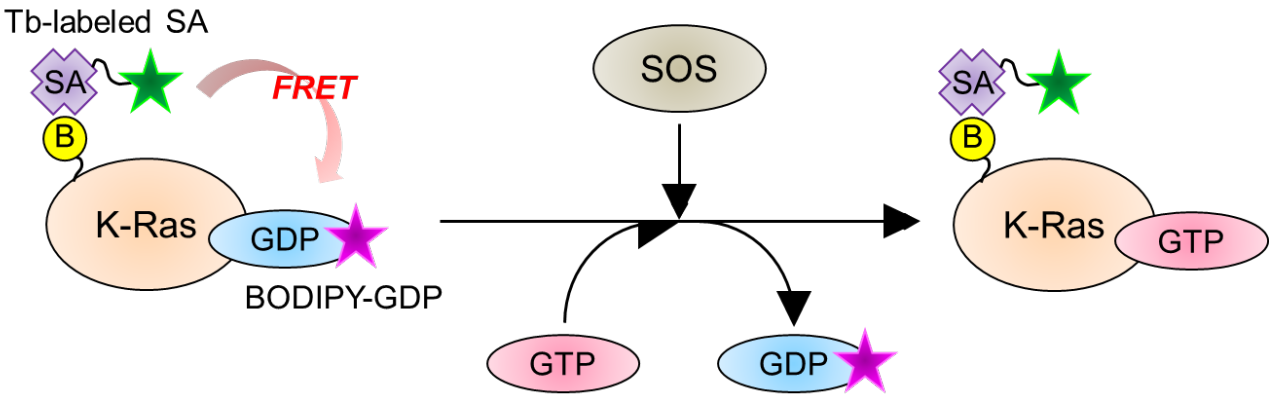

(B)

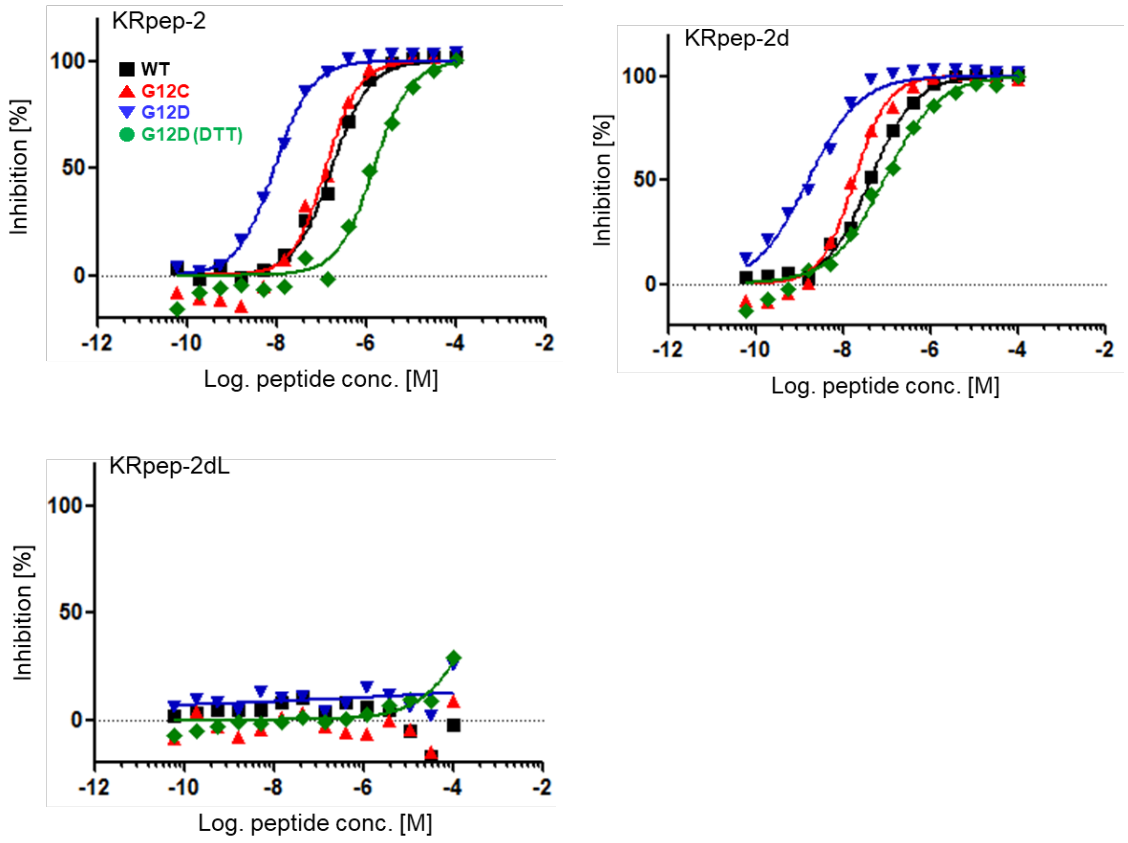

Figure 2-4. Enzyme inhibition activities of peptides. (A) Assay scheme. (B) Inhibition-activity and -selectivity of synthetic peptides.

(A)

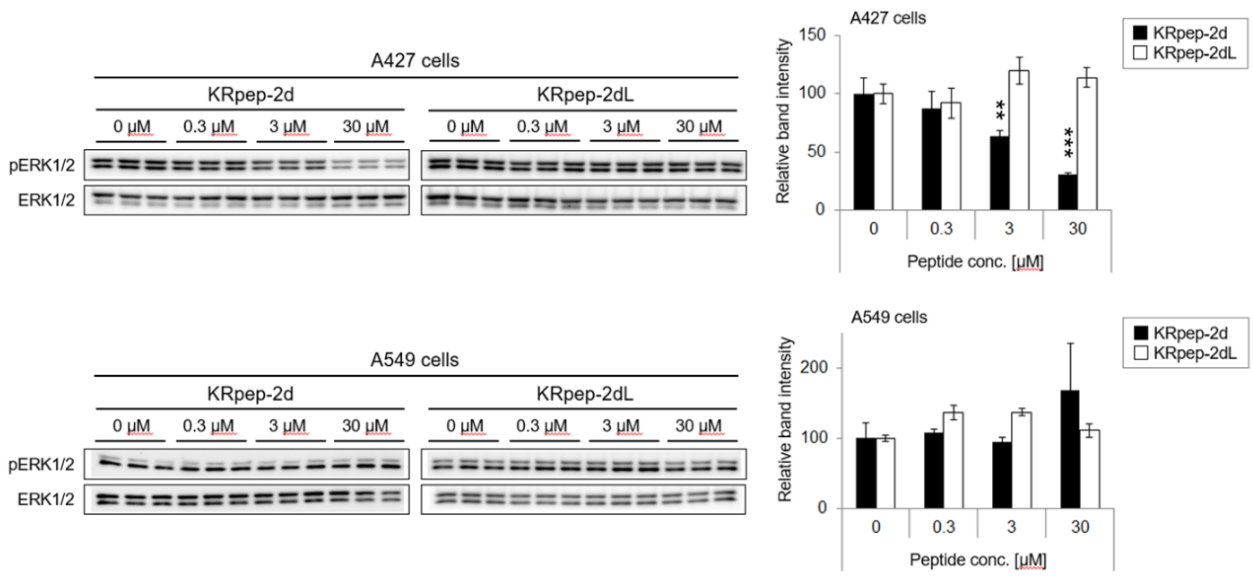

(B)

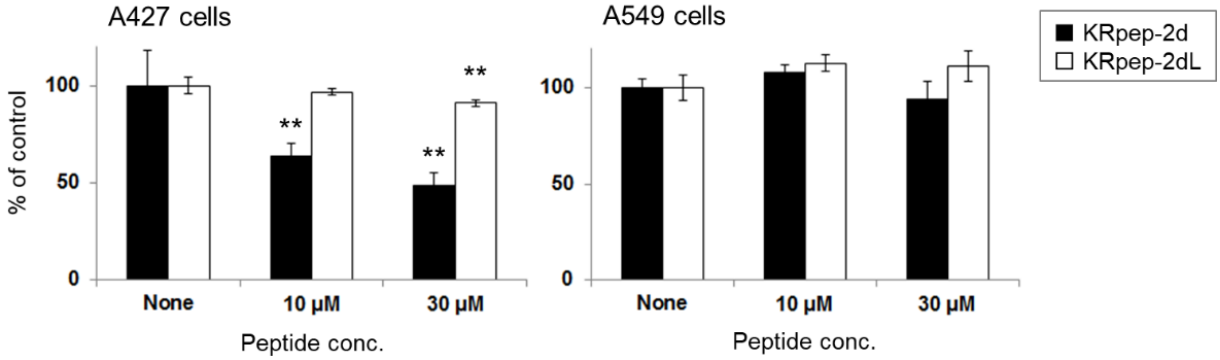

Figure 2-5. Inhibition activities of peptides towards K-Ras in A427 (K-Ras(G12D)) and A549 (K-Ras(G12C)) cells. Inhibition activity of synthetic peptides on (A) phosphorylation of ERK and (B) cell-proliferation. Data are means ± SD (n = 3, $^{**}P < 0.005$, $^{***}P < 0.0005$ by Williams test).

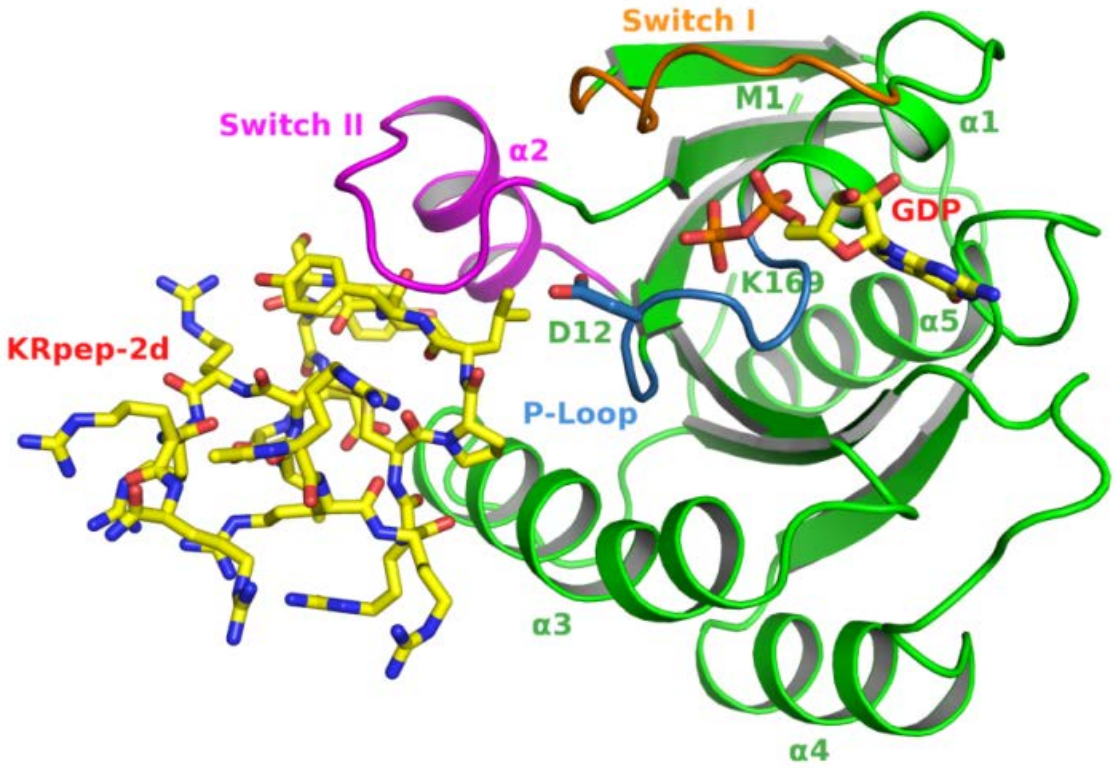

Figure 2-6. A ribbon diagram of the K-Ras(G12D)–KRpep-2d complex. GDP and KRpep-2d are depicted as yellow stick models, with Switch I, Switch II, and the P-loop indicated in orange, magenta, and blue, respectively.

(A)

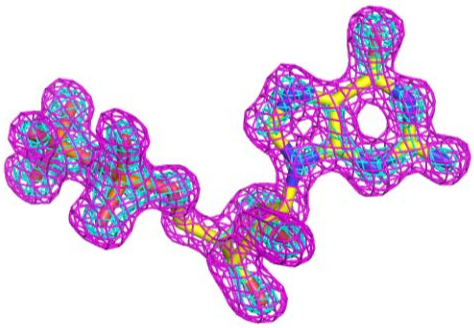

(B)

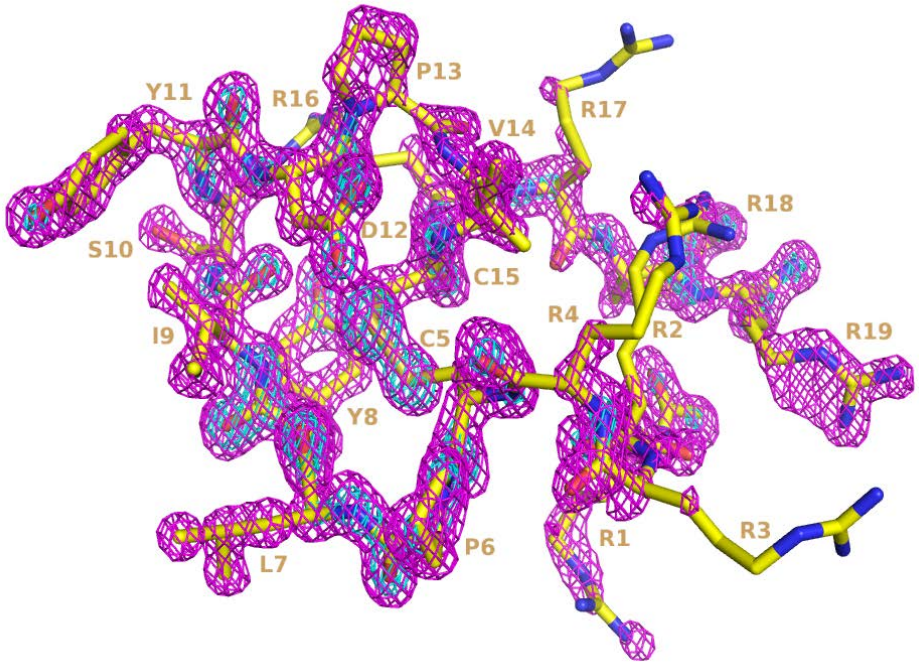

Figure 2-7. The $F_{obs}-F_{calc}$ electron density omit map contoured at 3σ within the vicinity of (A) GDP and (B) KRpep-2d.

(A)

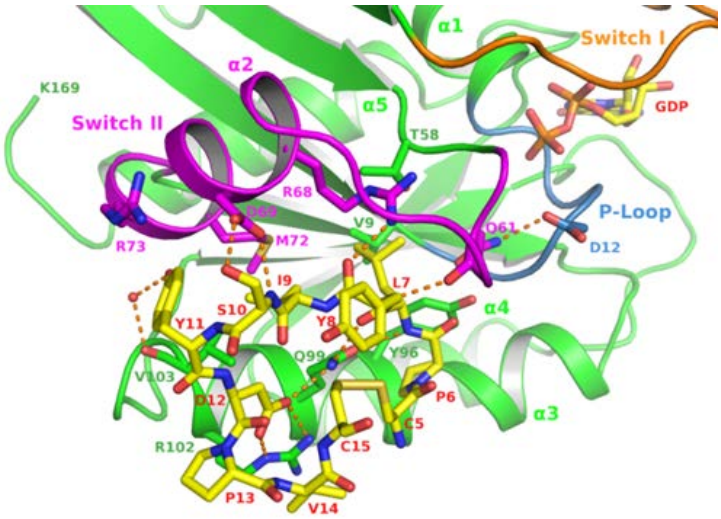

(B)

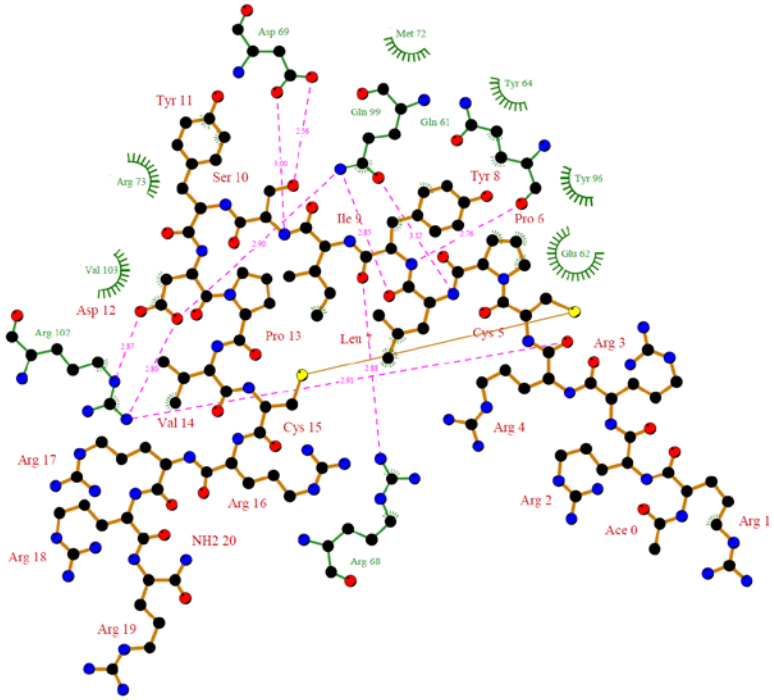

Figure 2-8. Binding interaction of KRpep-2d with K-Ras(G12D). (A) The color scheme is as described for Figure 1. Orange dashed lines indicate hydrogen bonds. Arginine residues at both termini of the peptide were excluded for clarity. (B) Schematic diagram of the K-Ras(G12D)−KRpep-2d interactions. Hydrogen bonds are depicted as dot lines.

(A)

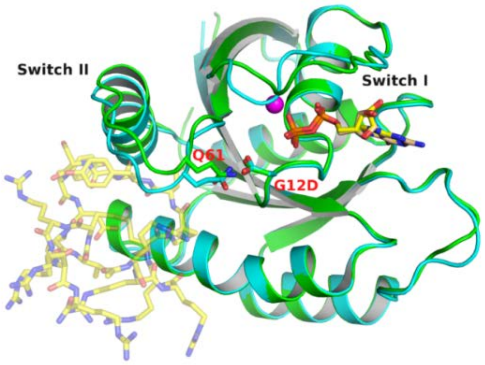

(B)

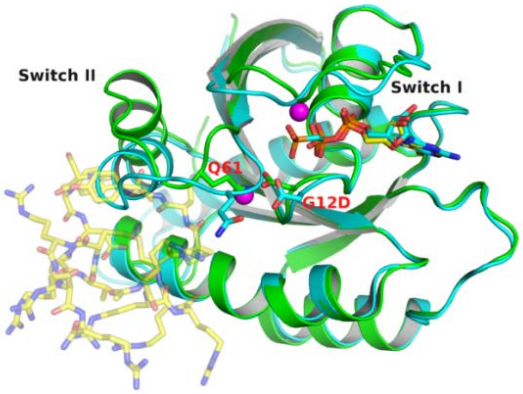

(C)

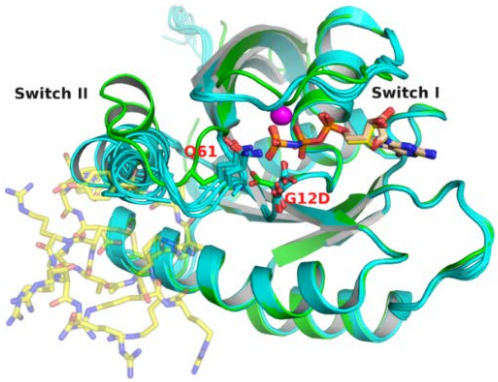

Figure 2-9. Structural comparison of the K-Ras(G12D)−GDP−KRpep-2d (green) complex with other K-Ras complexes (cyan). (A) The K-Ras(G12D) −GDP complex (PDB code 4EPR). (B) The K-Ras(G12D)−GMPPCP complex (PDB code 4DSN). (C) The K-Ras(G12D)−GMPPNP complex (PDB code 5USJ). All six monomers in the crystallographic asymmetric unit are superimposed. KRpep-2d is shown transparently for clarity. The magnesium ions are represented as magenta spheres.

(A)

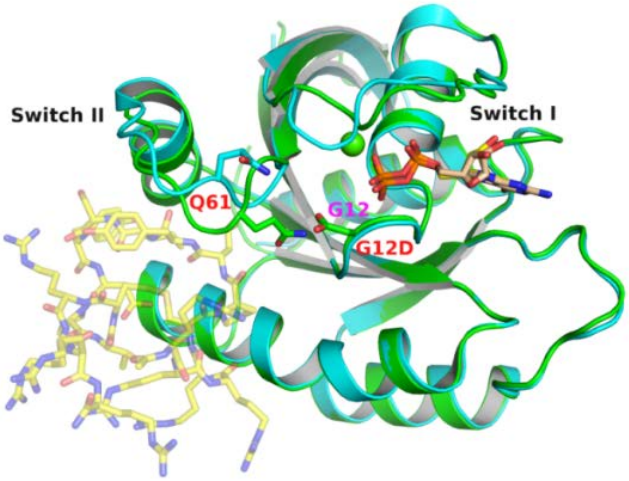

(B)

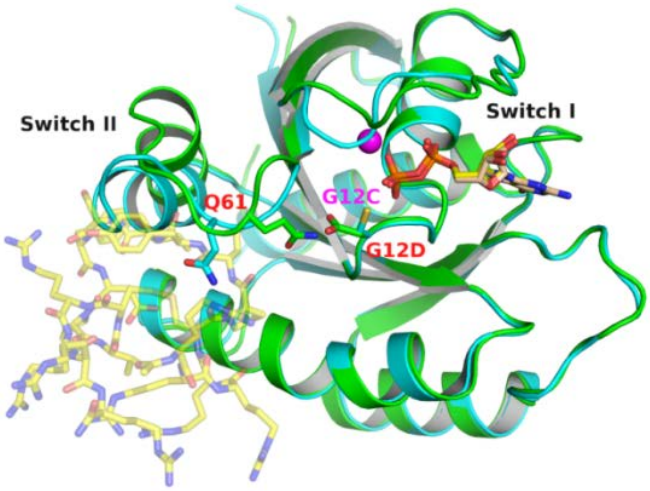

Figure 2-10. Structural comparison of the K-Ras(G12D)−GDP−KRpep-2d (green) complex with other K-Ras complexes (cyan). (A) The K-Ras(WT)−GDP complex (PDB code 4LPK). (B) The K-Ras(G12C)−GDP complex (PDB code 4LDJ). KRpep-2d is shown transparently for clarity. The magnesium and calcium ions are represented as magenta and green spheres, respectively.

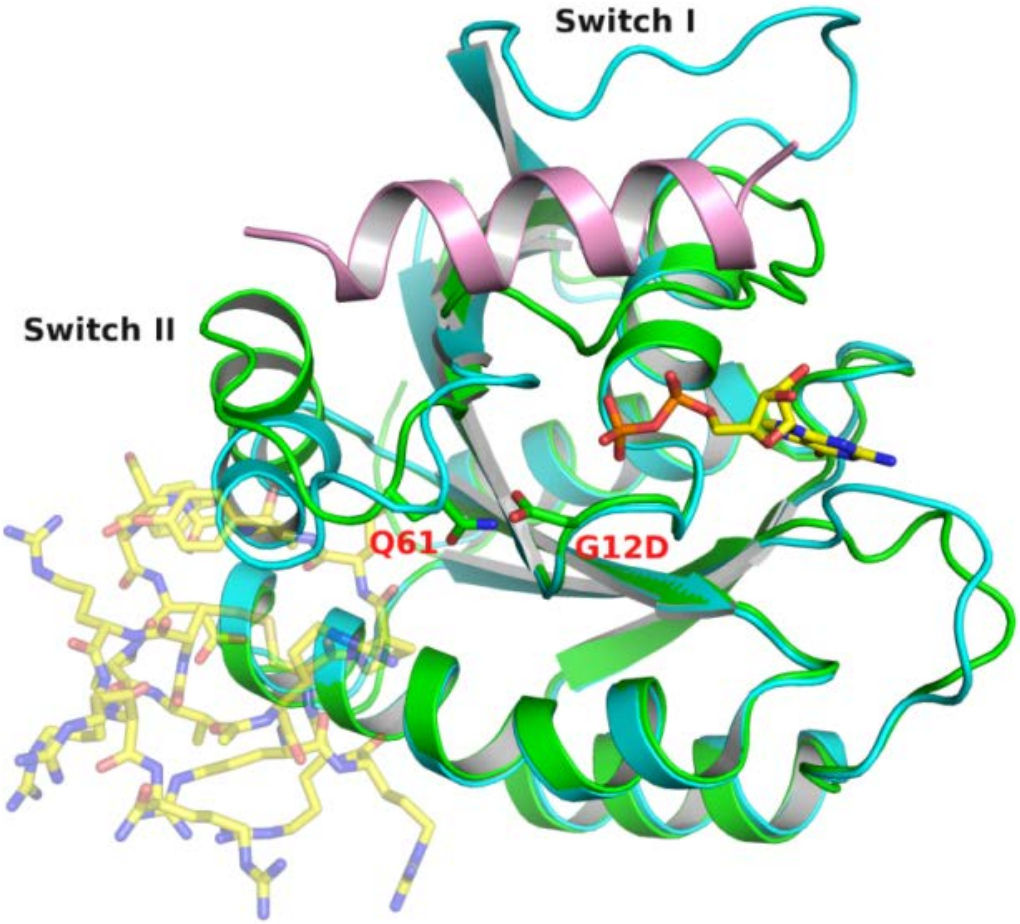

Figure 2-11. Structural comparison of the K-Ras(G12D)–GDP–KRpep-2d (green) complex with other Ras complexes (cyan). The H-Ras–SOS complex (PDB code 1NVW).

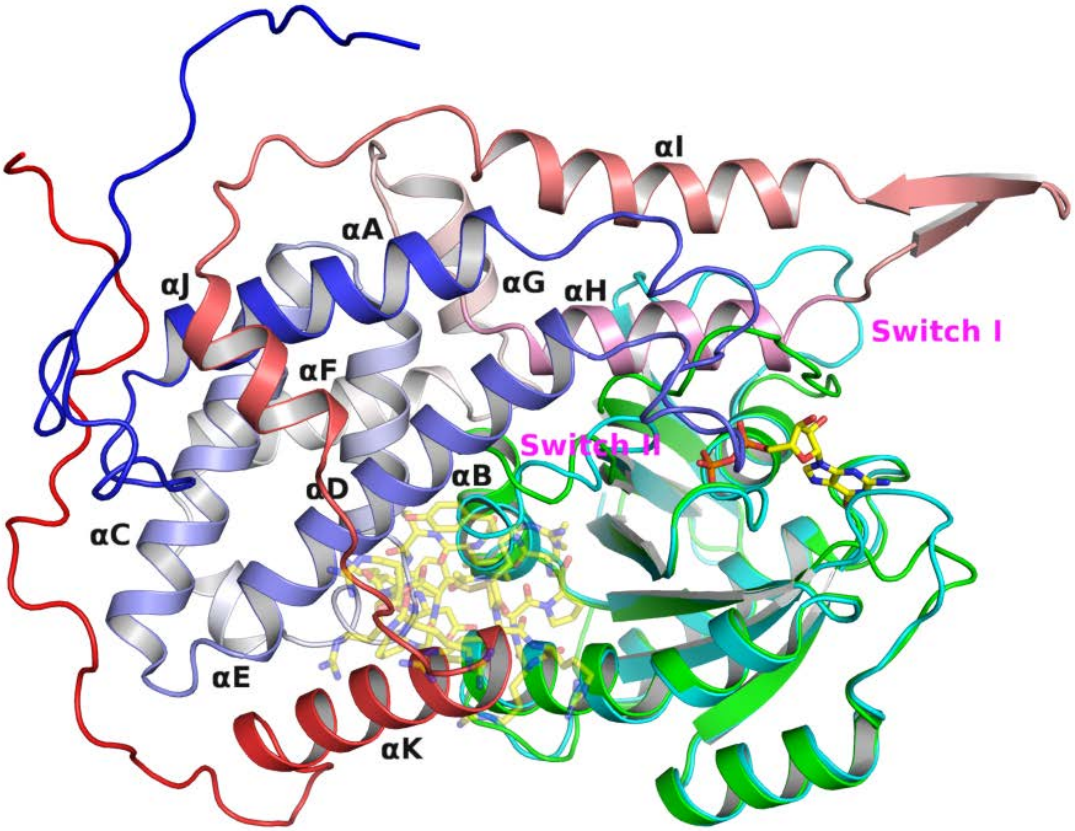

Figure 2-12. Structural comparison of the K-Ras(G12D)−GDP−KRpep-2d (green) complex with the H-Ras−SOS complex (cyan) (PDB code 1NVW). KRpep-2d is shown transparently for clarity. Only the cdc25 domain of SOS (residues 750−1046) is drawn for clarity. The carbon atoms of the cdc25 domain of SOS are drawn with a spectrum of colors ranging from blue to red.

(A)

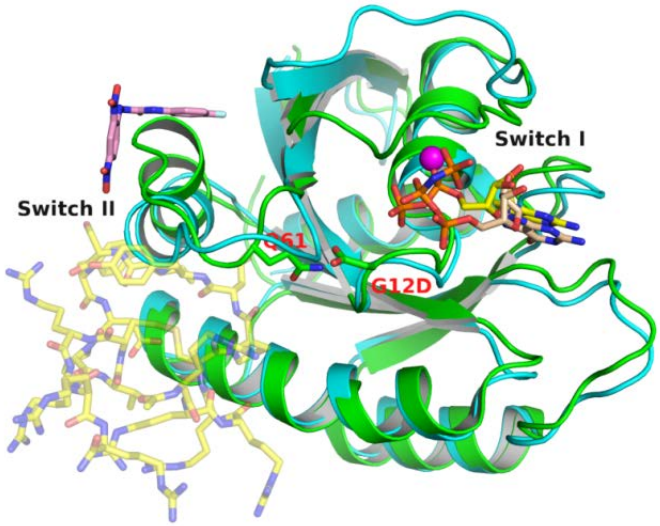

(B)

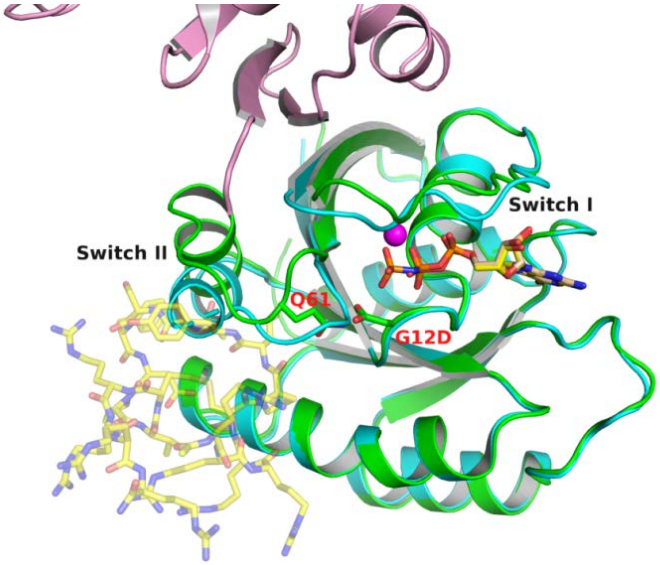

Figure 2-13. Structural comparison of the K-Ras(G12D)−GDP−KRpep-2d (green) complex with other K-Ras complexes (cyan). (A) The H-Ras(T35S)−GMPPNP−Kobe2601 complex (PDB code 2LWI). (B) The H-Ras–GMPPNP−Raf-RBD complex (PDB code 4G0N). The magnesium ions are represented by magenta spheres. KRpep-2d is shown transparently for clarity. The carbon atoms of Kobe2601 and Raf-RBD are colored pink.

General Discussion

In this study, I identified inhibitors against 2 PPIs with distinct properties using a screening method that was optimized for the properties of these PPIs. In chapter I, I describe fragment-based screening against BCL6, which interacts with BcoR and has predicted hot spots, and in chapter II, detail the results of phage display screening against K-Ras, which interacts with SOS1 via conformational changes. Both of these proteins are associated with cancer and BCL6 has also been associated with autoimmune disease.

PPIs are an attractive class of target for drug discovery. However, the discovery of inhibitors that disrupt PPI functions remains extremely difficult in contrast with typical drug targets, and functional inhibitors of PPIs are commonly produced as antibodies. Herein, I identify potent compounds that can target PPIs in cells. In the last 20 years, various trials have been performed with molecules that target PPIs, and considerable progress has been made in the identification of small molecule-based PPI inhibitors. However, this research area requires more sophisticated strategies to discover more effective and versatile inhibitors.

The BCL6–BcoR PPI is widely considered a therapeutic target for cancer and autoimmune disease, and the following biophysical properties have been described: 1) the PPI buried surface area is moderate at approximately 2000 $Å^2$, 2) BCL6 interacts with a loop region of BCoR without causing conformational changes, 3) the affinity of BCL6–BCoR binding is weak at about 10 μM, 4), reported HTS resulted in low affinity compounds only. Taken together, these data suggest the absence of hot spots on BCL6.

In contrast, the present phage display screen identified a high affinity linear peptide that binds to BCL6, and the high affinity binding of this peptide remained after truncation.[28] Hence, fragment-based screening against BCL6 is a feasible approach to searching for hot spots on BCL6. In subsequent SPR-based fragment screens, I identify

fragment **1** and SPR and X-ray analyses revealed that fragment **1** competes with the BcoR peptide and binds to a hotspot on BCL6. Using iterative synthesis with information regarding complex structures, I generated compound **7**, which has a K_D value in the nanomolar order and inhibits PPIs in cells.

In a previous study, I identified the BCL6-binding peptide with high affinity using a phage display screen and expected to find compounds with high affinity. In particular, although the affinity of BcoR peptide for BCL6 is weak (2-digit micromolar), I found compound **7** with an affinity of 2-digit nanomolar. Therefore, the affinity of the endogenous ligand will not indicate the required affinity of artificial ligands, especially if the target PPI has hot spots.

The present experiments identified BCL6 binding fragments apart from fragment **1**, but complex structures of these fragments were not solved and although SAR were investigated, these were poorly elucidated in the absence of complex structures. Because fragments generally have extremely low binding affinities (around 1 mM), related compounds are expected to have low affinity, and the resulting nonspecific binding effects and insolubility at high concentrations hampers accurate quantitative measurements of binding affinities. Hence, future analyses of complex structures will be central to the discovery of potent PPI inhibitory compounds from fragment-based screening.

The K-Ras–SOS1 PPI has potential as a therapeutic target for cancer and has 1) a large buried surface area of over 3000 $Å^2$ and 2) is mediated in part by conformational changes. However, 3) SAR of screened inhibitory fragments have not been reported. I selected phage display screening to identify inhibitors of this target and considered allosteric mimetics of the SOS1 peptide as likely candidates. Accordingly, I conducted phage display screening against K-Ras (G12D) to generate linear and cyclic peptides that bind K-Ras. These experiments revealed several cyclic peptides, and among them, KRpep-2d had nanomolar binding affinity for K-Ras (G12D) in SPR

experiments. Furthermore, the present data show that this peptide competes with SOS1 and is selective of K-Ras forms (G12C, WT, and GTP-form). To elucidate binding modes of KRpep-2d, I conducted alanine scanning and X-ray crystal structure analyses and showed that KRpep-2d binds the allosteric site of K-Ras.

The present study identified unique cyclic peptides that bind the allosteric site of K-Ras, but these were not linear peptides that bind allosteric or the orthosteric sites, suggesting that K-Ras does not have hot spots that can be targeted by selective small molecules. K-Ras binding compounds were discovered previously, and although SAR were investigated, no improvements of affinity were reported,[64, 66, 89] further indicating the absence of hot spots in K-Ras. The cyclic peptide KRpep-2d is more complex than other typical small molecule inhibitors, and high affinity and selective compounds such as KRpep-2d will need to have complexity. Hence, macrocyclic libraries or small molecular mimetics of KRpep-2d will be useful for the generation of compounds that bind K-Ras with high affinity and selectivity.

In this study, I discovered inhibitors of 2 PPI targets using biophysics-based screening methods that monitor binding activity. In contrast with typical inhibitors of drug targets, compound **7** and KRpep-2d both have unique properties, and bind hot spot and allosteric sites, respectively. These observations indicate that PPIs are feasible drug targets in the early stages of drug discovery. Hector Gracis-Seisdedos *et al.* previously suggested that hot spots play important roles in the self-assembly of proteins.[90] Thus, compounds that bind these sites may be important tools for further investigations of protein interactions.

Strategies for drug discovery depend on the properties of target PPIs, particularly because the properties of PPIs are more varied than typical target classes. In the schematic below (Figure 3-1), I suggest a work-flow for the

discovery of PPI inhibitors on the basis of the evidence provided in this study. Target PPIs can be classified according to the presence of hot spots and these can be predicted according to preferences for conformational changes, and with respect to epitopes of partner proteins, in addition to buried surface areas. When the presence of hot spots remains unclear, phage display screening can be used to discover linear peptides and to shorten them for fragment-based screening, which is suitable because high affinity compounds are likely for hot spot sites. Conversely, when cyclic peptides are considered in isolation, targeted proteins tend to identify steric ligands. Therefore, libraries of macrocyclic compounds and peptide mimetics are suitable for compound screening against these PPIs.

In this work-flow, biophysical methods play important roles in screening and analysis of interactions, and recent developments of these methods have been remarkable. In the future, the possibility of discovering PPI inhibitors will increase, and the next step is to optimize identified PPI inhibitors and develop them to the clinical stage. Due to the use of distinct discovery strategies, it is likely that compounds with distinct profiles will be discovered, and these will be more complex than those of typical drug targets. Therefore, novel medicinal chemistry approaches will be necessary.

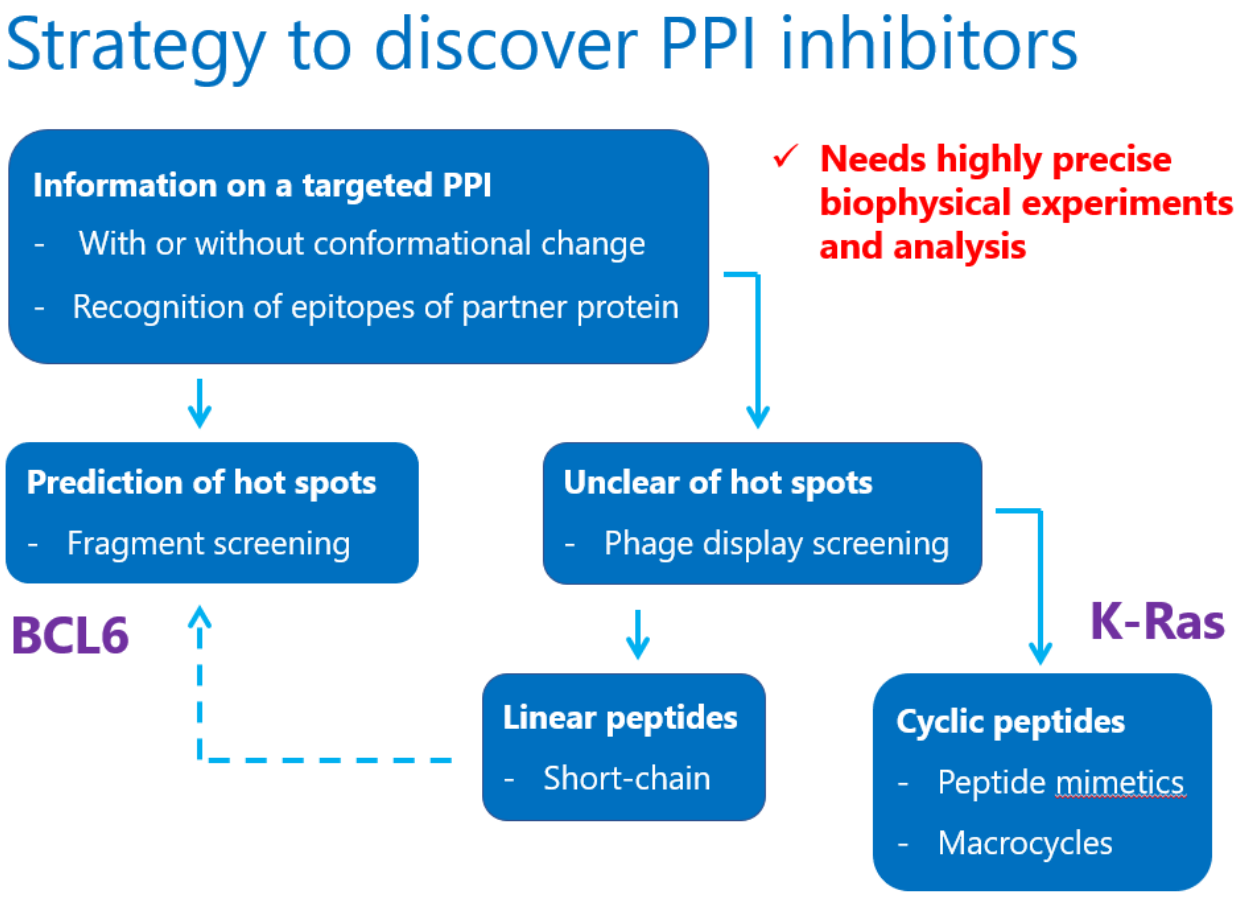

Figure 3-1. Work-flow to discover PPI inhibitors.

Acknowledgements

I am deeply grateful to Associate Professor Ryusuke Niwa, University of Tsukuba, for being in charge of this dissertation, and for valuable discussions through my doctoral program.

I also thank to Professors Yuji Inagaki, Kazuto Nakata, and Associate Professor Kentaro Nakano, for their appropriate advice during the preparation of this dissertation.

I appreciate Dr. Mutsuyoshi Matsushita and Dr. Yuji Matsuzaki, Japan Tabacco Inc., for understanding and supporting on my doctoral program. I also thank my coworkers at Japan Tabacco Inc., for their understanding during my doctoral program.

I am very thankful to Dr. Satoshi Sogabe, Dr. Kotaro Sakamoto, and Dr. Nozomu Sakai, for guiding my work and valuable discussions through my work. I also wish to thank my coworkers at Takeda Pharmaceutical Company Limited, for their contributions and helpful supports.

Finally, I would like to appreciate my family for supporting my life in University of Tsukuba.

References

1. Stumpf, M. P.; Thorne, T.; de Silva, E.; Stewart, R.; An, H. J.; Lappe, M.; Wiuf, C., Estimating the size of the human interactome. *Proc Natl Acad Sci U S A* **2008,** *105* (19), 6959-64.

2. Lo Conte, L.; Chothia, C.; Janin, J., The atomic structure of protein-protein recognition sites. *J Mol Biol* **1999,** *285* (5), 2177-98.

3. Renaud, J.-P.; Chung, C.-w.; Danielson, U. H.; Egner, U.; Hennig, M.; Hubbard, R. E.; Nar, H., Biophysics in drug discovery: impact, challenges and opportunities. *Nature Reviews Drug Discovery* **2016,** *15*, 679.

4. Lovering, F.; Bikker, J.; Humblet, C., Escape from flatland: increasing saturation as an approach to improving clinical success. *J Med Chem* **2009,** *52* (21), 6752-6.

5. Sidhu, S. S.; Fairbrother, W. J.; Deshayes, K., Exploring protein-protein interactions with phage display. *Chembiochem : a European journal of chemical biology* **2003,** *4* (1), 14-25.

6. Higueruelo, A. P.; Jubb, H.; Blundell, T. L., Protein-protein interactions as druggable targets: recent technological advances. *Curr Opin Pharmacol* **2013,** *13* (5), 791-6.

7. Oltersdorf, T.; Elmore, S. W.; Shoemaker, A. R.; Armstrong, R. C.; Augeri, D. J.; Belli, B. A.; Bruncko, M.; Deckwerth, T. L.; Dinges, J.; Hajduk, P. J.; Joseph, M. K.; Kitada, S.; Korsmeyer, S. J.; Kunzer, A. R.; Letai, A.; Li, C.; Mitten, M. J.; Nettesheim, D. G.; Ng, S.; Nimmer, P. M.; O'Connor, J. M.; Oleksijew, A.; Petros, A. M.; Reed, J. C.; Shen, W.; Tahir, S. K.; Thompson, C. B.; Tomaselli, K. J.; Wang, B.; Wendt, M. D.; Zhang, H.; Fesik, S. W.; Rosenberg, S. H., An inhibitor of Bcl-2 family proteins induces regression of solid tumours. *Nature* **2005,** *435* (7042), 677-81.

8. Smith, M. C.; Gestwicki, J. E., Features of protein-protein interactions that translate into potent inhibitors: topology, surface area and affinity. *Expert Rev Mol Med* **2012,** *14,* e16.

9. Arkin, M. R.; Tang, Y.; Wells, J. A., Small-molecule inhibitors of protein-protein interactions: progressing toward the reality. *Chem Biol* **2014,** *21* (9), 1102-14.

10. Raj, M.; Bullock, B. N.; Arora, P. S., Plucking the high hanging fruit: a systematic approach for targeting protein-protein interactions. *Bioorg Med Chem* **2013,** *21* (14), 4051-7.

11. Jochim, A. L.; Arora, P. S., Systematic analysis of helical protein interfaces reveals targets for synthetic inhibitors. *ACS Chem Biol* **2010,** *5* (10), 919-23.

12. Scott, D. E.; Bayly, A. R.; Abell, C.; Skidmore, J., Small molecules, big targets: drug discovery faces the protein-protein interaction challenge. *Nat Rev Drug Discov* **2016,** *15* (8), 533-50.

13. Lawson, A. D. G.; MacCoss, M.; Heer, J. P., Importance of Rigidity in Designing Small Molecule Drugs To Tackle Protein-Protein Interactions (PPIs) through Stabilization of Desired Conformers. *J Med Chem* **2017**.

14. Andrei, S. A.; Sijbesma, E.; Hann, M.; Davis, J.; O'Mahony, G.; Perry, M. W. D.; Karawajczyk, A.; Eickhoff, J.; Brunsveld, L.; Doveston, R. G.; Milroy, L. G.; Ottmann, C., Stabilization of protein-protein interactions in drug discovery. *Expert Opin Drug Discov* **2017,** *12* (9), 925-940.

15. Clackson, T.; Wells, J. A., A hot spot of binding energy in a hormone-receptor interface. *Science* **1995,** *267* (5196), 383-6.

16. Bogan, A. A.; Thorn, K. S., Anatomy of hot spots in protein interfaces. *J Mol Biol* **1998,** *280* (1), 1-9.

17. DeLano, W. L.; Ultsch, M. H.; de Vos, A. M.; Wells, J. A., Convergent solutions to binding at a protein-

protein interface. *Science* **2000,** *287* (5456), 1279-83.

18. Turnbull, A.; Boyd, S.; Walse, B., Fragment-based drug discovery and protein–protein interactions. *Research and Reports in Biochemistry* **2014**.

19. Genick, C. C.; Wright, S. K., Biophysics: for HTS hit validation, chemical lead optimization, and beyond. *Expert Opin Drug Discov* **2017,** *12* (9), 897-907.

20. Folmer, R. H., Integrating biophysics with HTS-driven drug discovery projects. *Drug Discov Today* **2016,** *21* (3), 491-8.

21. Dahl, G.; Akerud, T., Pharmacokinetics and the drug-target residence time concept. *Drug Discov Today* **2013,** *18* (15-16), 697-707.

22. Schuetz, D. A.; Richter, L.; Amaral, M.; Grandits, M.; Grädler, U.; Musil, D.; Buchstaller, H.-P.; Eggenweiler, H.-M.; Frech, M.; Ecker, G. F., Ligand Desolvation Steers On-Rate and Impacts Drug Residence Time of Heat Shock Protein 90 (Hsp90) Inhibitors. *Journal of Medicinal Chemistry* **2018**.

23. Johnson, C. N.; Erlanson, D. A.; Jahnke, W.; Mortenson, P. N.; Rees, D. C., Fragment-to-Lead Medicinal Chemistry Publications in 2016. *J Med Chem* **2018,** *61* (5), 1774-1784.

24. Wielens, J.; Headey, S. J.; Rhodes, D. I.; Mulder, R. J.; Dolezal, O.; Deadman, J. J.; Newman, J.; Chalmers, D. K.; Parker, M. W.; Peat, T. S.; Scanlon, M. J., Parallel screening of low molecular weight fragment libraries: do differences in methodology affect hit identification? *J Biomol Screen* **2013,** *18* (2), 147-59.

25. Larsson, E. A.; Jansson, A.; Ng, F. M.; Then, S. W.; Panicker, R.; Liu, B.; Sangthongpitag, K.; Pendharkar, V.; Tai, S. J.; Hill, J.; Dan, C.; Ho, S. Y.; Cheong, W. W.; Poulsen, A.; Blanchard, S.; Lin, G. R.;

Alam, J.; Keller, T. H.; Nordlund, P., Fragment-based ligand design of novel potent inhibitors of tankyrases. *J Med Chem* **2013,** *56* (11), 4497-508.

26. Wells, J. A.; McClendon, C. L., Reaching for high-hanging fruit in drug discovery at protein–protein interfaces. *Nature* **2007,** *450*, 1001.

27. Sakamoto, K.; Adachi, Y.; Komoike, Y.; Kamada, Y.; Koyama, R.; Fukuda, Y.; Kadotani, A.; Asami, T.; Sakamoto, J. I., Novel DOCK2-selective inhibitory peptide that suppresses B-cell line migration. *Biochem Biophys Res Commun* **2017,** *483* (1), 183-190.

28. Sakamoto, K.; Sogabe, S.; Kamada, Y.; Sakai, N.; Asano, K.; Yoshimatsu, M.; Ida, K.; Imaeda, Y.; Sakamoto, J. I., Discovery of high-affinity BCL6-binding peptide and its structure-activity relationship. *Biochem Biophys Res Commun* **2017,** *482* (2), 310-316.

29. Nevola, L.; Giralt, E., Modulating protein-protein interactions: the potential of peptides. *Chem Commun (Camb)* **2015,** *51* (16), 3302-15.

30. Huynh, K. D.; Fischle, W.; Verdin, E.; Bardwell, V. J., BCoR, a novel corepressor involved in BCL-6 repression. *Genes Dev* **2000,** *14* (14), 1810-23.

31. Dent, A. L.; Shaffer, A. L.; Yu, X.; Allman, D.; Staudt, L. M., Control of inflammation, cytokine expression, and germinal center formation by BCL-6. *Science* **1997,** *276* (5312), 589-92.

32. Linterman, M. A.; Vinuesa, C. G., Signals that influence T follicular helper cell differentiation and function. *Semin Immunopathol* **2010,** *32* (2), 183-96.

33. Nurieva, R. I.; Chung, Y.; Martinez, G. J.; Yang, X. O.; Tanaka, S.; Matskevitch, T. D.; Wang, Y. H.;

Dong, C., Bcl6 mediates the development of T follicular helper cells. *Science* **2009,** *325* (5943), 1001-5.

34. Xin, N.; Fu, L.; Shao, Z.; Guo, M.; Zhang, X.; Zhang, Y.; Dou, C.; Zheng, S.; Shen, X.; Yao, Y.; Wang, J.; Wang, J.; Cui, G.; Liu, Y.; Geng, D.; Xiao, C.; Zhang, Z.; Dong, R., RNA interference targeting Bcl-6 ameliorates experimental autoimmune myasthenia gravis in mice. *Mol. Cell. Neurosci.* **2014,** *58*, 85-94.

35. Parekh, S.; Privé, G.; Melnick, A., Therapeutic targeting of the BCL6 oncogene for diffuse large B-cell lymphomas. *Leuk Lymphoma* **2008,** *49* (5), 874-82.

36. Duy, C.; Hurtz, C.; Shojaee, S.; Cerchietti, L.; Geng, H.; Swaminathan, S.; Klemm, L.; Kweon, S. M.; Nahar, R.; Braig, M.; Park, E.; Kim, Y. M.; Hofmann, W. K.; Herzog, S.; Jumaa, H.; Koeffler, H. P.; Yu, J. J.; Heisterkamp, N.; Graeber, T. G.; Wu, H.; Ye, B. H.; Melnick, A.; Müschen, M., BCL6 enables Ph+ acute lymphoblastic leukaemia cells to survive BCR-ABL1 kinase inhibition. *Nature* **2011,** *473* (7347), 384-8.

37. Ahmad, K. F.; Melnick, A.; Lax, S.; Bouchard, D.; Liu, J.; Kiang, C. L.; Mayer, S.; Takahashi, S.; Licht, J. D.; Privé, G. G., Mechanism of SMRT corepressor recruitment by the BCL6 BTB domain. *Mol Cell* **2003,** *12* (6), 1551-64.

38. Cerchietti, L. C.; Ghetu, A. F.; Zhu, X.; Da Silva, G. F.; Zhong, S.; Matthews, M.; Bunting, K. L.; Polo, J. M.; Fares, C.; Arrowsmith, C. H.; Yang, S. N.; Garcia, M.; Coop, A.; Mackerell, A. D., Jr.; Prive, G. G.; Melnick, A., A small-molecule inhibitor of BCL6 kills DLBCL cells in vitro and in vivo. *Cancer Cell* **2010,** *17* (4), 400-11.

39. Cardenas, M. G.; Yu, W.; Beguelin, W.; Teater, M. R.; Geng, H.; Goldstein, R. L.; Oswald, E.; Hatzi, K.; Yang, S. N.; Cohen, J.; Shaknovich, R.; Vanommeslaeghe, K.; Cheng, H.; Liang, D.; Cho, H. J.; Abbott, J.; Tam, W.; Du, W.; Leonard, J. P.; Elemento, O.; Cerchietti, L.; Cierpicki, T.; Xue, F.; MacKerell, A. D., Jr.;

Melnick, A. M., Rationally designed BCL6 inhibitors target activated B cell diffuse large B cell lymphoma. *J. Clin. Invest.* **2016,** *126* (9), 3351-62.

40. Cerchietti, L. C.; Yang, S. N.; Shaknovich, R.; Hatzi, K.; Polo, J. M.; Chadburn, A.; Dowdy, S. F.; Melnick, A., A peptomimetic inhibitor of BCL6 with potent antilymphoma effects in vitro and in vivo. *Blood* **2009,** *113* (15), 3397-405.

41. Evans, S. E.; Goult, B. T.; Fairall, L.; Jamieson, A. G.; Ko Ferrigno, P.; Ford, R.; Schwabe, J. W.; Wagner, S. D., The ansamycin antibiotic, rifamycin SV, inhibits BCL6 transcriptional repression and forms a complex with the BCL6-BTB/POZ domain. *PLoS One* **2014,** *9* (3), e90889.

42. Whittaker, M., Picking up the pieces with FBDD or FADD: invest early for future success. *Drug Discov. Today* **2009,** *14* (13-14), 623-4.

43. Varnes, J. G.; Geschwindner, S.; Holmquist, C. R.; Forst, J.; Wang, X.; Dekker, N.; Scott, C. W.; Tian, G.; Wood, M. W.; Albert, J. S., Fragment-assisted hit investigation involving integrated HTS and fragment screening: Application to the identification of phosphodiesterase 10A (PDE10A) inhibitors. *Bioorg Med Chem Lett* **2016,** *26* (1), 197-202.

44. Hopkins, A. L.; Keserü, G. M.; Leeson, P. D.; Rees, D. C.; Reynolds, C. H., The role of ligand efficiency metrics in drug discovery. *Nat Rev Drug Discov* **2014,** *13* (2), 105-21.

45. Perspicace, S.; Banner, D.; Benz, J.; Muller, F.; Schlatter, D.; Huber, W., Fragment-based screening using surface plasmon resonance technology. *J. Biomol. Screen.* **2009,** *14* (4), 337-49.

46. Otwinowski, Z.; Minor, W., Processing of X-ray diffraction data collected in oscillation mode. In

Macromolecular Crystallography, part A, Carter, C. W. J.; Sweet, R. M., Eds. Academic Press: New York, 1997; Vol. 276, pp 307-326.

47. Vagin, A.; Teplyakov, A., MOLREP: an Automated Program for Molecular Replacement. *Journal of Applied Crystallography* **1997,** *30* (6), 1022-1025.

48. Collaborative Computational Project, N., The CCP4 suite: programs for protein crystallography. *Acta Crystallogr. D Biol. Crystallogr.* **1994,** *50* (Pt 5), 760-3.

49. Murshudov, G. N.; Skubák, P.; Lebedev, A. A.; Pannu, N. S.; Steiner, R. A.; Nicholls, R. A.; Winn, M. D.; Long, F.; Vagin, A. A., REFMAC5 for the refinement of macromolecular crystal structures. *Acta Crystallogr D Biol Crystallogr* **2011,** *67* (Pt 4), 355-67.

50. Emsley, P.; Lohkamp, B.; Scott, W. G.; Cowtan, K., Features and development of Coot. *Acta Crystallogr D Biol Crystallogr* **2010,** *66* (Pt 4), 486-501.

51. Chen, V. B.; Arendall, W. B.; Headd, J. J.; Keedy, D. A.; Immormino, R. M.; Kapral, G. J.; Murray, L. W.; Richardson, J. S.; Richardson, D. C., MolProbity: all-atom structure validation for macromolecular crystallography. *Acta Crystallogr D Biol Crystallogr* **2010,** *66* (Pt 1), 12-21.

52. Elinder, M.; Geitmann, M.; Gossas, T.; Källblad, P.; Winquist, J.; Nordström, H.; Hämäläinen, M.; Danielson, U. H., Experimental validation of a fragment library for lead discovery using SPR biosensor technology. *J Biomol Screen* **2011,** *16* (1), 15-25.

53. Hämäläinen, M. D.; Zhukov, A.; Ivarsson, M.; Fex, T.; Gottfries, J.; Karlsson, R.; Björsne, M., Label-free primary screening and affinity ranking of fragment libraries using parallel analysis of protein panels. *J Biomol*

Screen **2008,** *13* (3), 202-9.

54. Nordström, H.; Gossas, T.; Hämäläinen, M.; Källblad, P.; Nyström, S.; Wallberg, H.; Danielson, U. H., Identification of MMP-12 inhibitors by using biosensor-based screening of a fragment library. *J Med Chem* **2008,** *51* (12), 3449-59.

55. Navratilova, I.; Macdonald, G.; Robinson, C.; Hughes, S.; Mathias, J.; Phillips, C.; Cook, A., Biosensor-based approach to the identification of protein kinase ligands with dual-site modes of action. *J Biomol Screen* **2012,** *17* (2), 183-93.

56. Nordin, H.; Jungnelius, M.; Karlsson, R.; Karlsson, O. P., Kinetic studies of small molecule interactions with protein kinases using biosensor technology. *Anal Biochem* **2005,** *340* (2), 359-68.

57. Stenlund, P.; Frostell-Karlsson, A.; Karlsson, O. P., Studies of small molecule interactions with protein phosphatases using biosensor technology. *Anal Biochem* **2006,** *353* (2), 217-25.

58. Hopkins, A. L.; Groom, C. R.; Alex, A., Ligand efficiency: a useful metric for lead selection. *Drug Discov Today* **2004,** *9* (10), 430-1.

59. Baines, A. T.; Xu, D.; Der, C. J., Inhibition of Ras for cancer treatment: the search continues. *Future Med Chem* **2011,** *3* (14), 1787-808.

60. Cox, A. D.; Fesik, S. W.; Kimmelman, A. C.; Luo, J.; Der, C. J., Drugging the undruggable RAS: Mission possible? *Nat Rev Drug Discov* **2014,** *13* (11), 828-51.

61. Ledford, H., Cancer: The Ras renaissance. *Nature* **2015,** *520* (7547), 278-80.

62. Karnoub, A. E.; Weinberg, R. A., Ras oncogenes: split personalities. *Nat Rev Mol Cell Biol* **2008,** *9* (7),

517-31.

63. Ford, B.; Boykevisch, S.; Zhao, C.; Kunzelmann, S.; Bar-Sagi, D.; Herrmann, C.; Nassar, N., Characterization of a Ras mutant with identical GDP- and GTP-bound structures. *Biochemistry* **2009,** *48* (48), 11449-57.

64. Ostrem, J. M.; Shokat, K. M., Direct small-molecule inhibitors of KRAS: from structural insights to mechanism-based design. *Nat Rev Drug Discov* **2016,** *15* (11), 771-785.

65. Ostrem, J. M.; Peters, U.; Sos, M. L.; Wells, J. A.; Shokat, K. M., K-Ras(G12C) inhibitors allosterically control GTP affinity and effector interactions. *Nature* **2013,** *503* (7477), 548-51.

66. Patgiri, A.; Yadav, K. K.; Arora, P. S.; Bar-Sagi, D., An orthosteric inhibitor of the Ras-Sos interaction. *Nat Chem Biol* **2011,** *7* (9), 585-7.

67. Wu, X.; Upadhyaya, P.; Villalona-Calero, M. A.; Briesewitz, R.; Pei, D., Inhibition of Ras-Effector Interaction by Cyclic Peptides. *Medchemcomm* **2013,** *4* (2), 378-382.

68. Upadhyaya, P.; Qian, Z.; Selner, N. G.; Clippinger, S. R.; Wu, Z.; Briesewitz, R.; Pei, D., Inhibition of Ras signaling by blocking Ras-effector interactions with cyclic peptides. *Angew Chem Int Ed Engl* **2015,** *54* (26), 7602-6.

69. Trinh, T. B.; Upadhyaya, P.; Qian, Z.; Pei, D., Discovery of a Direct Ras Inhibitor by Screening a Combinatorial Library of Cell-Permeable Bicyclic Peptides. *ACS Comb Sci* **2016,** *18* (1), 75-85.

70. Sakamoto, K.; Ito, Y.; Mori, T.; Sugimura, K., Interaction of human lactoferrin with cell adhesion molecules through RGD motif elucidated by lactoferrin-binding epitopes. *J Biol Chem* **2006,** *281* (34), 24472-8.

71. Sakamoto, K.; Ito, Y.; Hatanaka, T.; Soni, P. B.; Mori, T.; Sugimura, K., Discovery and characterization of a peptide motif that specifically recognizes a non-native conformation of human IgG induced by acidic pH conditions. *J Biol Chem* **2009,** *284* (15), 9986-93.

72. Otwinowski, Z.; Minor, W., Processing of X-ray diffraction data collected in oscillation mode. *Methods Enzymol* **1997,** *276*, 307-26.

73. McCoy, A. J.; Grosse-Kunstleve, R. W.; Adams, P. D.; Winn, M. D.; Storoni, L. C.; Read, R. J., Phaser crystallographic software. *J Appl Crystallogr* **2007,** *40* (Pt 4), 658-674.

74. Collaborative Computational Project, N. m., The CCP4 suite: programs for protein crystallography. *Acta Crystallogr D Biol Crystallogr* **1994,** *50* (Pt 5), 760-3.

75. Winn, M. D.; Isupov, M. N.; Murshudov, G. N., Use of TLS parameters to model anisotropic displacements in macromolecular refinement. *Acta Crystallogr D Biol Crystallogr* **2001,** *57* (Pt 1), 122-33.

76. Wallace, A. C.; Laskowski, R. A.; Thornton, J. M., LIGPLOT: a program to generate schematic diagrams of protein-ligand interactions. *Protein Eng* **1995,** *8* (2), 127-34.

77. Perspicace, S.; Banner, D.; Benz, J.; Müller, F.; Schlatter, D.; Huber, W., Fragment-based screening using surface plasmon resonance technology. *J Biomol Screen* **2009,** *14* (4), 337-49.

78. Vartanian, S.; Bentley, C.; Brauer, M. J.; Li, L.; Shirasawa, S.; Sasazuki, T.; Kim, J. S.; Haverty, P.; Stawiski, E.; Modrusan, Z.; Waldman, T.; Stokoe, D., Identification of mutant K-Ras-dependent phenotypes using a panel of isogenic cell lines. *J Biol Chem* **2013,** *288* (4), 2403-13.

79. Niida, A.; Sasaki, S.; Yonemori, K.; Sameshima, T.; Yaguchi, M.; Asami, T.; Sakamoto, K.; Kamaura,

M., Investigation of the structural requirements of K-Ras(G12D) selective inhibitory peptide KRpep-2d using alanine scans and cysteine bridging. *Bioorg Med Chem Lett* **2017,** *27* (12), 2757-2761.

80. Lu, S.; Jang, H.; Nussinov, R.; Zhang, J., The Structural Basis of Oncogenic Mutations G12, G13 and Q61 in Small GTPase K-Ras4B. *Sci Rep* **2016,** *6*, 21949.

81. Boriack-Sjodin, P. A.; Margarit, S. M.; Bar-Sagi, D.; Kuriyan, J., The structural basis of the activation of Ras by Sos. *Nature* **1998,** *394* (6691), 337-43.

82. Burns, M. C.; Howes, J. E.; Sun, Q.; Little, A. J.; Camper, D. V.; Abbott, J. R.; Phan, J.; Lee, T.; Waterson, A. G.; Rossanese, O. W.; Fesik, S. W., High-throughput screening identifies small molecules that bind to the RAS:SOS:RAS complex and perturb RAS signaling. *Analytical Biochemistry* **2018,** *548*, 44-52.

83. Winter, J. J.; Anderson, M.; Blades, K.; Brassington, C.; Breeze, A. L.; Chresta, C.; Embrey, K.; Fairley, G.; Faulder, P.; Finlay, M. R.; Kettle, J. G.; Nowak, T.; Overman, R.; Patel, S. J.; Perkins, P.; Spadola, L.; Tart, J.; Tucker, J. A.; Wrigley, G., Small molecule binding sites on the Ras:SOS complex can be exploited for inhibition of Ras activation. *J Med Chem* **2015,** *58* (5), 2265-74.

84. Shima, F.; Yoshikawa, Y.; Ye, M.; Araki, M.; Matsumoto, S.; Liao, J.; Hu, L.; Sugimoto, T.; Ijiri, Y.; Takeda, A.; Nishiyama, Y.; Sato, C.; Muraoka, S.; Tamura, A.; Osoda, T.; Tsuda, K.; Miyakawa, T.; Fukunishi, H.; Shimada, J.; Kumasaka, T.; Yamamoto, M.; Kataoka, T., In silico discovery of small-molecule Ras inhibitors that display antitumor activity by blocking the Ras-effector interaction. *Proc Natl Acad Sci U S A* **2013,** *110* (20), 8182-7.

85. Fetics, S. K.; Guterres, H.; Kearney, B. M.; Buhrman, G.; Ma, B.; Nussinov, R.; Mattos, C., Allosteric

effects of the oncogenic RasQ61L mutant on Raf-RBD. *Structure* **2015,** *23* (3), 505-516.

86. Pham, W.; Kircher, M. F.; Weissleder, R.; Tung, C. H., Enhancing membrane permeability by fatty acylation of oligoarginine peptides. *Chembiochem* **2004,** *5* (8), 1148-51.

87. MacRaild, C. A.; Illesinghe, J.; van Lierop, B. J.; Townsend, A. L.; Chebib, M.; Livett, B. G.; Robinson, A. J.; Norton, R. S., Structure and activity of (2,8)-dicarba-(3,12)-cystino alpha-ImI, an alpha-conotoxin containing a nonreducible cystine analogue. *J Med Chem* **2009,** *52* (3), 755-62.

88. Hargittai, B.; Solé, N. A.; Groebe, D. R.; Abramson, S. N.; Barany, G., Chemical syntheses and biological activities of lactam analogues of alpha-conotoxin SI. *J Med Chem* **2000,** *43* (25), 4787-92.

89. Burns, M. C.; Sun, Q.; Daniels, R. N.; Camper, D.; Kennedy, J. P.; Phan, J.; Olejniczak, E. T.; Lee, T.; Waterson, A. G.; Rossanese, O. W.; Fesik, S. W., Approach for targeting Ras with small molecules that activate SOS-mediated nucleotide exchange. *Proc Natl Acad Sci U S A* **2014,** *111* (9), 3401-6.

90. Garcia-Seisdedos, H.; Empereur-Mot, C.; Elad, N.; Levy, E. D., Proteins evolve on the edge of supramolecular self-assembly. *Nature* **2017,** *548* (7666), 244-247.